GA–A27657

ADVANCED DESIGN — ARIES

Final Report for the Period October 1, 2010 Through September 27, 2013

by
A.D. TURNBULL, H.E. ST JOHN, L.L. LAO, M. CHOI, R.J. BUTTERY,
S.P. SMITH, P.B. SNYDER, G.M. STAEBLER, G.L. JACKSON, and K.R. SCHULTZ

Work supported by
the US Department of Energy
under DE-FC02-04ER54698

NOVEMBER 2013

GENERAL ATOMICS

DISCLAIMER

GA–A27657

ADVANCED DESIGN — ARIES

Final Report for the Period October 1, 2010 Through September 27, 2013

by
A.D. TURNBULL, H.E. ST JOHN, L.L. LAO, M. CHOI, R.J. BUTTERY,
S.P. SMITH, P.B. SNYDER, G.M. STAEBLER, G.L. JACKSON, and K.R. SCHULTZ

GENERAL ATOMICS PROJECT 30200
NOVEMBER 2013

1. Introduction

Current research on tokamak edge plasma physics and plasma-facing component engineering points to a substantial gap between our best predictions of the heat and particle fluxes leaving the edge plasma and the maximum allowable fluxes that would result in a reliable and economically attractive power plant. The Research Needs Workshop (ReNeW) effort [1] and the previous ARIES study described these gaps and defined research needed to close the gaps. As a follow-on to this, a new study was initiated whose goals were to seek credible, self-consistent solutions appropriate for a commercial power plant and define more precisely the remaining gaps. The plan was to revisit selected previous ARIES design studies and re-optimize using the UCSD Systems Code with the latest understanding of the physics and technology challenges and options. The four designs selected consisted of the four combinations of conventional and advanced physics and conventional and advanced technology (conservative and "aggressive").

In support of this goal, General Atomics (GA) initially contributed in-house physics expertise in fusion and plasma physics, and the expertise in technology to provide detailed technical input. In particular, GA contracted to provide an evaluation of the prospects for small edge localized mode (ELM) or ELM-free operation in a reactor scenario, based on current understanding of these regimes. Additional supplementary funding was provided to perform a simulation to confirm that the baseline design points obtained from the ARIES Systems Code optimization are self-consistent, stable, steady state solutions. This entailed adapting and coupling the current state-of-the-art plasma physics models for equilibrium, transport, stability, and current drive to the design configurations. This became the primary effort and the planned efforts on small ELM and ELM-free operation were substantially curtailed. However, due to severe funding cuts in FY2013 the simulations for the advanced option were also scaled back and the simulations for the conventional option were not performed.

In Sec. 2 the ELM-free and small ELM work is described. Section 3 describes the self-consistent steady state calculations for the advanced physics and technology design point. Several iterations were done and, since each iteration revealed new issues that needed resolving, the individual iterations are described in some detail. Section 4 describes the additional efforts as part of the ARIES Team in communicating the research results through workshops, meetings, and publications, as well as additional technical contributions from GA that were solicited explicitly by the ARIES Team.

2. Prospects of Small ELM and No ELM Reactor Operation

A plan for evaluating options for small ELM and ELM-free scenarios in a reactor was formulated. The plan required identifying the critical features producing the desired ELM characteristics in current experiments, evaluating their ideal stability to edge modes and correlating this with the observed ELM behavior. Accordingly, ELM-free and small ELM regimes were evaluated for their potential for a reactor scenario using the most up to date knowledge available.

The most promising ELM-free regimes are the Quasi-H mode (QH-mode) [2] and related options such as the enhanced D-alpha (EDA) mode in C-Mod [3], and ELM-free operation induced by an imposed non-axisymmetric resonant magnetic perturbation (RMP) [4,5], and Li conditioning [6]. In addition, the I-mode option observed in C-Mod [7] was found to have favorable characteristics. The major issue in each of these is the somewhat restricted operational ranges where ELM-free operation is obtained but the physics responsible is not yet well-known and recent progress suggests some of the current range restrictions might be removed. The currently most promising small ELM regime is obtained through triggering small frequent ELMs via paced pellets [8]. The major competitor is the Type II regime [9], which is also characterized by smaller more frequent ELMs. In both, divertor heat loads in present experiments are reduced by an order of magnitude compared to standard Type I ELMs. Type III ELMs [10] were also considered. The major issues for the Type II and Type III ELM options are the present lack of reproducibility; as in the ELM-free options, the physics behind the transition to these states is largely unknown. A final option considered on the basis of experiments in DIII-D involves controlling ELM size through higher order cross-section shaping [11].

Ultimately, the scaling of the essential characteristics needs to be determined for each option. If a reasonable estimate of the scaling is known, reactor configurations scaled from the current experiments can be produced and their edge stability evaluated. However, given the current lack of understanding of the physics mechanisms this may not be possible. The original plan therefore involved taking representative discharges for each regime from the respective machines and determining the essential features of the profiles and other characteristics, in order to describe the dependence of ELM type and size, and to scale the configurations using the density and temperature profiles from the respective discharges but with the ARIES profiles — particularly the elevated q profile in the ARIES advanced physics designs.

As mentioned in Sec. 1, however, the scope was considerably reduced in order to focus on the self-consistent simulations. The effort was correspondingly refocused on just a few particular options and scaling calculations were not attempted. Instead, an overall assessment of the prospects was reached from a literature search. The original proposal was also modified to reflect continuing developments. In particular, several options that showed some promise initially were eliminated from consideration. The remaining options still suggest promise and progress has been made in expanding the operational limits as well as in understanding the mechanisms involved in terms of the peeling-ballooning stability model. The Li conditioning option was analyzed in some detail and is discussed in the following subsection. This option shows significant promise for ELM control, since experimentally, these discharges range from ELMing to infrequent ELMs to ELM-free, depending on level of Li conditioning. Consequently, a significant effort was initiated to understand the physics involved by attempting to evaluate the stability of actual NSTX discharges with the aim of establishing the characteristics of the pedestal density and temperature profiles and their proximity to the peeling and ballooning stability boundaries. While the aim of establishing the characteristics of the pedestal profiles and their proximity to the peeling and ballooning stability boundaries was not completed, the exercise was useful in improving code capabilities that can be useful for future efforts. This is discussed in Sec. 2.1.

For the QH-mode and RMP induced ELM-free options, progress has been made in expanding the operational limits as well as in understanding the mechanisms involved, specifically in terms of the peeling-ballooning stability model [12]. These are briefly discussed in Sec. 2.2. The recently discovered I-Mode on C-Mod, characterized by ELM-free operation with L-mode particle confinement but H-mode energy confinement, offers a new potential scenario if it can be scaled to a reactor. This is discussed in Sec. 2.3. In addition, the recent promising results on controlling ELMs by pacing with small pellets are discussed briefly in Sec. 2.4. Section 2.5 briefly discusses the remaining options. The overall limited conclusions from the study are discussed briefly in Sec. 2.6.

2.1. Li Conditioning

A significant effort was initiated to understand the physics involved in the Li conditioning experiments in NSTX [6] by attempting to evaluate the stability of actual NSTX discharges. In collaboration with R. Maingi [Princeton Plasma Physics Laboratory (PPPL)], stability calculations were done for several NSTX discharges with Li conditioning, ranging from reduced ELMs to ELM-free. Four equilibria were obtained from NSTX and the stability was calculated using the GATO code [13]. The cases were from NSTX discharge #129015, which had no lithium and was a Type I ELMing H-mode, discharges #129030 and #129031 with significant lithium, and also Type I

ELMing H-mode, but with a low ELM frequency which transitions to ELM-free soon after the Li application, and discharge #129038, with a large amount of lithium, and which was completely ELM-free. The calculations were performed for toroidal mode number n = 1, 2, 3, and 4 for each discharge equilibrium. All were found to be stable, despite the observed ELM activity in the discharges with either no or limited Li conditioning. This was confirmed by independent calculations using the KINX code [14] by Medvedev at the Keldysh Institute. Independent calculations using the PPPL PEST code [15] found instabilities, in disagreement with the GATO and KINX calculations. The difference between the PEST and other code predictions was finally determined to be due to the fact that the PEST code cuts the edge region from the diverted equilibria at around 95% of the poloidal flux, effectively producing a different equilibrium, particularly in the edge which is the region of interest.

The GATO and KINX stability calculations are apparently in disagreement with the experimental observations of ELMs in the discharges with little or no lithium. However, the stability of edge modes is well known to be sensitive to the equilibrium details. The discrepancy is therefore thought to be due to insufficiently resolved edge profiles. In the absence of a more accurate equilibrium reconstruction, a detailed benchmark between the GATO code and the ELITE code [16] was first performed in order to ensure that the code predictions for the actual equilibrium provided are valid. The first test using an NSTX-like equilibrium with enhanced edge current density that yielded large unstable growth rates with ELITE, found remarkably good overall agreement in the mode growth rates and mode structures for $n > 8$. The GATO calculations find unstable edge modes from n = 3 up to n = 12. This is a particularly challenging case for both codes due to the small aspect ratio resulting in strong edge gradients and high edge q. The comparison was done for a cutoff in the equilibrium that is at 99% of the poloidal flux in order to lower the edge q to the same value ($q \sim 11.9$). The resonant poloidal mode numbers scale with $m \sim nq$ and toroidal coupling considerably extends this range so that extremely high radial and poloidal resolution is required to resolve the rational surfaces and the poloidal oscillations. For the ELITE code, the radius of convergence to the most unstable mode is small for these cases and an accurate initial guess is required. The vacuum calculation in the GATO code becomes increasingly less accurate with increased n and breaks down for $n > 15$.

Despite the challenges for both codes, the growth rates for the most unstable edge mode were in agreement to within 10% to 20% for $7 < n < 12$ and a detailed comparison of the mode structure for the n=10 case showed remarkable agreement given that ELITE is a fourier based code and GATO is a global finite element code. For this, ELITE required up to $m = 130$ poloidal harmonics. GATO used a packed mesh of 400 flux surfaces and 800 poloidal angles to ensure resolution though the results were unchanged

to within a percent with a $N_\psi \times N_\chi = 200 \times 400$ mesh. For this initial benchmark case, the growth rates for the $n = 9$ and $n = 10$ ideal peeling-ballooning modes were compared and are shown in Table I. A direct comparison of the eigenmodes for $n = 10$ is shown in Fig. 1.

Table I
Calculated Growth Rates From the GATO and ELITE Codes for $n = 9$ and 10 for the NSTX Benchmark Equilibrium

N	GATO	ELITE
9	0.5677	0.5500
10	0.5853	0.5794

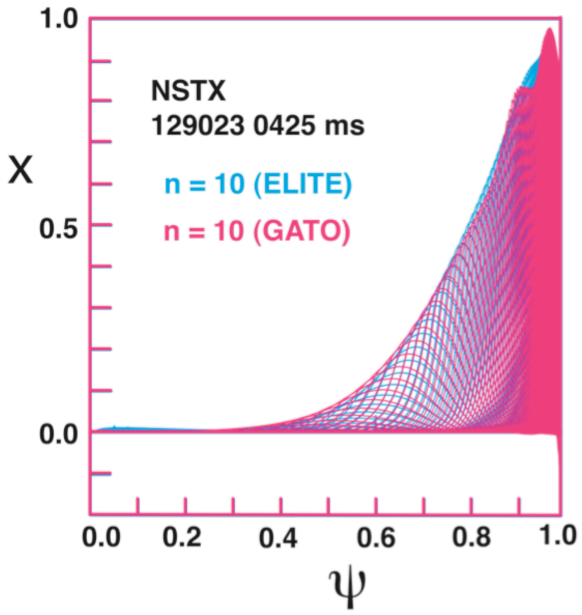

Fig. 1. Benchmark comparison of the $n = 10$ peeling-ballooning eigenfunctions $X = \xi \cdot \nabla\psi$ from ELITE (blue) and GATO (red).

A further technical complication arose in that subdominant modes were also found in both codes. In GATO these are all internal kinks unrelated to the expected edge localized modes, but for ELITE they have an edge component. This appears to be due to the fact that ELITE forces a finite edge displacement and vanishing on axis displacement; the code attempted to find the internal kinks but is constrained to impose the finite edge displacement. Since the ELITE code has some difficulties with the subdominant modes in this case, a benchmark study of a second case with a stronger edge instability was initiated, obtained by increasing the pedestal pressure by 250%. While the ELITE code finds clear unstable edge modes for $n>8$ in that case, the ELITE calculations still have

difficulties with some remaining internal modes. Therefore it was decided to revert to the original case and simply ignore the internal modes.

The benchmark provides confidence that the GATO calculations performed for the Li conditioned discharge equilibria are accurate and the discrepancy with the observed behavior resides in problems with the equilibrium reconstruction. Further progress on the analysis of these discharges requires a more accurate equilibrium reconstruction from NSTX using significantly higher resolution equilibria by the NSTX group, which is currently not technically possible.

2.2. QH-Mode and RMP ELM-free Options

Equilibria from DIII-D ELM-free Quiescent H-mode discharges [2] and discharges with an imposed RMP [4] were also obtained for stability analysis. However, due to the change in focus and the subsequent funding cuts, the stability analysis was not done. Instead, the literature was searched for data bearing on future prospects for these options. Most notably, for the QH-mode, progress has been made in expanding the operational limits as well as in understanding the mechanisms involved, specifically in terms of the peeling-ballooning stability model. The edge harmonic oscillation (EHO) [2] that appears concurrently with ELM-free operation appears to play a role in reducing the pedestal density, moving the operating point closer to the current-driven peeling mode region of the stability parameter space. While the plasmas appear to be stable to ideal modes, the EHO appears to be a peeling mode destabilized by strong edge rotation gradients, but which saturates nonlinearly at a small amplitude.

In contrast, for the RMP ELM-free option [4], the mechanism for ELM suppression is not yet understood but the RMP may play a similar role to the EHO of QH-mode. The most important element missing in the RMP option is that, while ELM-free operation is highly reproducible in any given machine, it is not very reproducible across machines and the mechanisms involved appear to be different in different machines. Experiments in ASDEX have reproduced aspects of the ELM suppression observed in DIII-D by non-axisymmetric external fields, though with some significant differences, most notably at much higher collisionality than is typical in the DIII-D experiments [17].

Additionally, experiments in DIII-D also demonstrated that by using external non-axisymmetric non-resonant magnetic fields (NRMFs) to generate counter-I_p torque, QH-mode operation can be achieved with ITER-relevant neutral beam torque while maintaining excellent energy confinement [5].

2.3. I-mode

The I-mode [7] is characterized by ELM-free operation with L-mode particle confinement but H-mode energy confinement. With L-mode particle transport, impurity accumulation is not an issue and the lack of a steep density pedestal appears to keep the overall edge pressure below the peeling-ballooning stability limit. Figure 2 shows the I-mode density and temperature profiles measured in C-Mod, compared to L-mode and H-mode profiles. This scenario therefore offers the potential of an L-mode like edge density pedestal and corresponding low particle confinement, with an H-mode like edge temperature pedestal with excellent energy confinement. This would resolve the issue of impurity accumulation. C-Mod data also shows that overall confinement degradation in I-mode is not a serious issue as the stored energy increases almost linearly with the heating power. The I-mode has been reliably reproduced in ASDEX-U and recent experiments in DIII-D appear to have reproduced a weak I-mode.

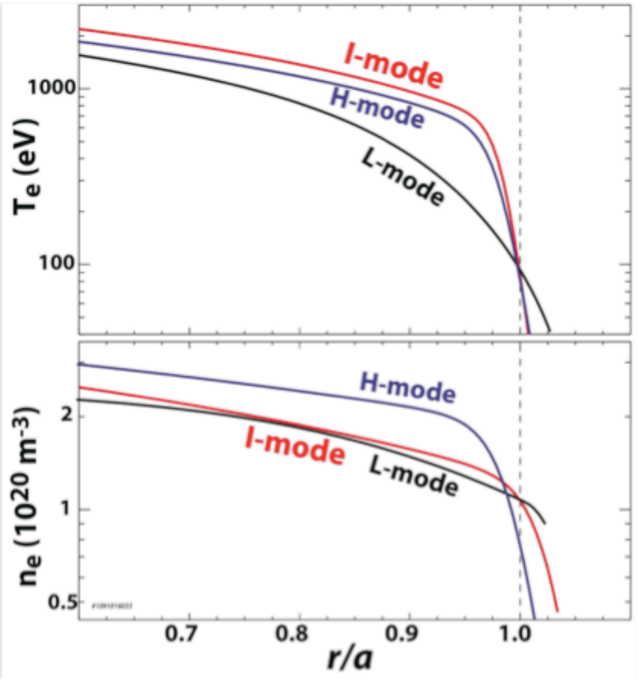

Fig. 2. Comparison of I-mode density and temperature profiles with L-mode and H-mode profiles (Courtesy D. Whyte MIT).

The I-mode is comparable in many ways to QH-mode, particularly in the presence of a continuous oscillation, similar to the EHO and thought to be related directly to the increased particle transport. A distinct contrast to QH-mode is that the regulation of the pedestal that keeps the discharge below the ELM threshold is apparently due to transport and not stability.

Analysis using simple scaling assumptions combined with modeling and experimental data suggests that I-mode can be scaled to ITER and to a reactor, as the power thresholds for the L-mode to I-mode and the I-mode to H-mode transitions appear to allow a feasible path to high gain with favorable density scaling [18]; the L-mode to I-mode transition power threshold scales proportional to electron density, n_e. By scaling the threshold heating power using this linear n_e scaling and an additional assumed scaling with the relative cross sections $P_{heat} \sim n_e\left(S_{ITER}/S_{C-Mod}\right)$, with $S_{ITER}/S_{C-Mod} \sim 9$, and taking into account the additional fusion alpha heating power in ITER, $P_{heat} = P_{ext} + P_{alpha}$, calculated from simulations using profiles from C-Mod I-mode discharges, it was found that I-mode can be accessed on ITER from low density at low external heating power, and the desired fusion power can be reached after the I-mode transition by then increasing the density concurrently with heating power. Recent experiments in C-Mod intended to test this scenario have confirmed that after a low density L-I transition, n_e could be increased 25% while remaining in I-mode [18].

2.4. ELM Pacing

One technique for reducing the impact of ELMs is by triggering smaller more frequent ELMs by injection of pellets of Deuterium. In DIII-D it was reported that new smaller millimeter sized pellets were effective in triggering ELMs up to a 30 Hz injection rate without affecting the average plasma density. Future experiments should allow up to 90 Hz pellet pacing. The data suggests that even smaller pellets may be used to trigger ELMs. This appears to be the most promising of the small ELM options.

2.5. Other Options

The EDA [3], and the Type II and III small ELM regimes [9,10], as well as the option of controlling ELM size with plasma shaping [11] appear to be unlikely to lead to a reactor solution since it seems unlikely that these options will be suitable in reactor conditions. The EDA option has limited operational range, has not been reproduced in experiments other than C-Mod, and does not appear to scale to a reactor. The Type II and Type III small ELM options also do not appear to be routinely reproducible or scalable to reactor conditions. This is particularly true for the Type III ELMs, though future developments may still change this conclusion for the Type II ELM option. In addition, the Type III option appears to be possible in a small operational range near the L to H transition and is associated with a significant reduction in plasma performance. Shaping to control ELMs with squareness on the other hand also appears to always result in a significant performance loss from reduced H-mode pedestal associated with the shaping changes and does not appear to yield sufficient ELM control. This is the most significant

drawback in this case. Nevertheless, some control might be affected in a reactor scenario from small changes in outboard squareness.

2.6. Conclusions

The remaining options still suggest promise and progress has been made in expanding the operational limits as well as in understanding the mechanisms involved in terms of the peeling-ballooning stability model. The Li Conditioning option shows significant promise for ELM control, since experimentally, these discharges range from ELMing to infrequent ELMs to ELM-free, depending on level of Li conditioning. However, ultimately, this option suffers from an issue common to several ELM-free options in that the good confinement in the absence of ELMs results in an accumulation of impurities since these are also well confined, and possibly even preferentially confined compared to deuterium ions; normally ELMs remove impurities and prevent this accumulation. In a burning plasma this would result in an accumulation of He ash that could quench the fusion reaction. Therefore, despite the potential flexibility this option would provide, in the present absence of a solution to the accumulation problem, the Li conditioning option should be considered as not viable as well.

Nevertheless, in recent experiments, it appears that ELMs are initiated in the ELM-free Li conditioned plasmas by adding a small non-axisymmetric field perturbation. This is in contrast to the DIII-D experiments where the non-axisymmetric fields induce an ELM-free phase under certain well-defined conditions. For NSTX the triggering of ELMs in conjunction with the Li conditioning could provide an additional tool to regulate the ELMs and thereby control both the impurity accumulation and the impact of ELMs on the divertor.

The QH-mode, RMP, and I-mode options do not appear to suffer from the issue of impurity accumulation. I-mode appears to be promising in terms of the basic requirements of good energy confinement and relatively poor particle confinement that allows ash removal but limited data exists across machines. The QH-mode option, either with or without NRMF is also promising and at least appears to be scalable to ITER. With the option of placing coils outside the vacuum vessel, the NRMF-assisted QH-mode may be particularly attractive. On the other hand, it is still not yet clear if the RMP option can be scaled to a reactor but an active research program is in place to determine at least the possibilities for this in ITER.

In summary, the major ELM-free options at present are the QH-mode and I-mode. The RMP option is also available but the scaling and technical considerations involved in placing active coils in the vicinity of a burning plasma require further work to resolve. However, the NRMF-assisted QH mode may alleviate many of the issues. With respect to

the small ELM options, pacing via pellets is currently the most promising solution. Nevertheless, the Type II ELM option may be viable if the scaling can be determined.

3. ARIES ACT1 Simulations

Simulations were designed to confirm that the baseline design points obtained from the Systems Code optimization are truly self-consistent, stable, steady-state solutions. This entailed adapting and coupling the current state-of-the-art plasma physics models for equilibrium, transport, stability, and current drive to the design configurations. As a first step, the computational tools were applied to reproduce and update the previously published ARIES advanced tokamak design results published in 2006 [19]. The tools were then applied to the new design with advanced physics and engineering identified from the recently upgraded Systems Code and denoted ACT 1, with the first iteration of the design designated ACT 1A. Subsequently the design was iterated within the Systems Code and the simulation steps were repeated for this design, denoted ACT 1B. Finally, the steps were repeated for the final design, which involved a change in major radius. In all four simulations, new challenges arose and the tools were refined as needed. Thus, the following describes each of the simulations since the lessons in each were applied to subsequent simulations. Section 3.1 describes the simulation procedure in detail. The new simulations for the 2006 design are described in Sec. 3.2 Sec. 3.3 discusses the simulations for the ACT 1A design. The ACT 1B simulations utilized two different transport models and these are discussed separately in Sec. 3.4 and 3.5. The simulations completed for the final design point are then described in Sec. 3.6. Section 3.7 summarizes the code modifications that were made in the course of this work that are available for future simulations and Sec. 3.8 and 3.9 briefly discuss the lessons learned and options for future work.

3.1. Simulation Procedure

The aim of the simulations was to repeat the previous 2006 effort [19] for the new updated ARIES-AT optimization, with improved tools and understanding. The analysis therefore involved coupled equilibrium, transport, current drive, fuelling, and stability calculations to obtain a steady state solution in a self-consistent simulation. The simulations use the same tools as used to model DIII-D and the Fusion Nuclear Science Facility (FSNF), providing a consistent up-to-date set of models and tools across the spectrum of current and planned facilities. The analysis initially intended to use the new optimized target configuration, ultimately with the latest core transport models, namely TGLF [20] in place of the GLF23 [21] analysis used in the earlier study, and coupled self-consistently to the edge H-mode pedestal model EPED1 [22]. The key improvement of the TGLF model over GLF23 is that it uses real shaped geometry instead of the shifted

circle equilibrium model and includes a refined model for the trapped electron mode (TEM). In the course of the work it was realized that the GLF23 model is in fact inadequate in these simulations. The TGLF code is prohibitively slow and it was decided to incorporate the Multi-Mode model [23] and code in place of GLF23. This will be described below.

The EPED1 model uses a realistic pedestal height and width determined from the predicted kinetic ballooning and ideal peeling-ballooning stability limits. This model has successfully predicted edge pedestal values over a wide range of experimental conditions in a number of current tokamaks extremely well [24]. It was used in the transport analyses presented here by supplying a constraint to the upper limit of the edge pedestal normalized beta. The pedestal parameters were obtained by constructing a population of equilibria with varying profiles and testing the stability for intermediate toroidal mode number n ideal modes and kinetic ballooning modes; optimization against both yields unique values for the height and width of the pedestal and a corresponding value for β_N^{ped}.

Ray tracing from the general ray tracing code GENRAY [25] was used during the initial simulations and it was planned to switch to full wave lower hybrid (LH) simulations for the final results. Also, in view of the improved resistive wall stability understanding gained in recent years, wall stabilization effects were to be evaluated. In particular the effects of wall stabilization at low rotation speeds and error fields coupled with angular momentum transport predictions were to be done. However, this was curtailed due to drastically reduced funding in the final year of the project, which prevented pursuing these and other scenarios.

The key technical issue in the simulation is that the core transport is stiff in the sense that the fluxes tend to depend on critical gradients, above which turbulence is increased due to micro-instability thresholds being exceeded. This generally means that the largest leverage to improving core confinement is from increasing the edge pedestal height. However, conversely, the H-mode pedestal and ELM physics depends crucially on the heat and particle fluxes coming from the core. For a given set of parameters, there is no guarantee that a self-consistent solution exists. Thus, some experimentation is likely needed to adjust the fuelling, current drive, and heating options.

The initial step in the simulation procedure required an initial equilibrium from the EFIT code [26] corresponding to the design point. Initially, pending completion of the Systems Code optimization, this took the equilibrium used in the 2000 ARIES study with $\beta_N = 5.7$ and the additional ad-hoc H-mode pedestal described in Ref. [19]. An initial simulation using the GENRAY code was done to reproduce the published current drive scenario. The first step beyond the published scenario was to incorporate a pedestal

optimization. The EPED1 model was used to predict the H-mode pedestal height and width, and provided a limiting value for the pedestal β_N^{ped}. This was iterated with a current-drive and transport simulation using the parallel version of the ONETWO code [27] coupled to GENRAY in order to align the profiles.

Ultimately, the iteration procedure is intended to be embedded in a β optimization to converge to the maximum stable β_N, with the ideal stability checked using GATO and the EFIT equilibria re-computed as needed. The overall optimization procedure is shown in Fig. 3. This shows the embedded iterations over equilibrium current drive, stability, and transport. The innermost iterations represent the self-consistent transport and equilibrium steps. These are embedded in an outer optimization loop.

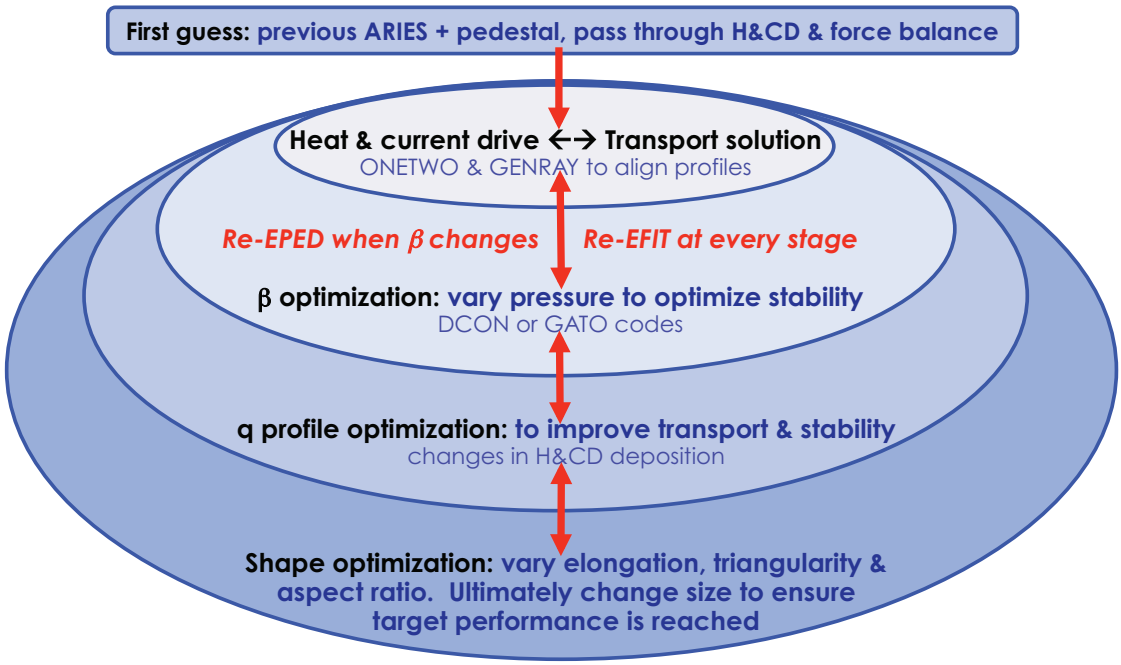

Fig. 3. Optimization procedure overview.

The IMFIT interface and its successor OMFIT [28] can also be used for the core loop of transport self consistently optimized for β_N with heating and current drive so that this optimization can be automated as much as possible. However, the final optimum from this procedure may not be acceptable for various reasons, for example, possibly requiring excessive external current drive. Adjustment of the safety factor profile will likely be needed to improve stability and current drive potential. This cannot be easily automated and will need some additional judgment. Subsequently, some shape optimization may also be necessary or desirable, specifically with respect to elongation, triangularity and aspect ratio. Size adjustments can also be made as needed.

In practice, the procedure was somewhat modified since the baseline configuration from the Systems Code continued evolving. Consequently, after each simulation for a given configuration, a new configuration from the Systems Code was substituted and the simulation repeated but with the lessons learned from the previous simulation incorporated in the new one. Essentially, an additional iteration loop was inserted in the scheme of Fig. 3 outside the innermost transport iteration loop where the new iteration involved the Systems Code re-optimization.

The first iteration of this process utilized the ARIES 2006 design in order to gain some initial experience with the effect of adding a consistent H-mode pedestal. Subsequently, three separate transport simulations were performed for three different optimized configurations from the Systems Code. The lessons obtained in each one were applied to varying degrees to subsequent simulations.

In the calculations for ARIES, the outer optimization was effectively performed via the Systems Code and, as a result of unexpected time and funding constraints, was consequently not invoked separately. Also, the incorporation into OMFIT was not completed. However, the computational tools were developed and linked in order to be able to realize this step in future simulations.

3.2. ARIES AT 2006

A partially consistent equilibrium, transport, current drive and stability analysis was performed originally in 2000 for the ARIES design and published in Ref. [19]. In that design, an *ad-hoc* pedestal was added to the equilibrium obtained from a self-consistent analysis of an L-mode scenario but assuming H-mode confinement. The current drive simulations used the L-mode edge conditions. Thus, the design was not truly self-consistent. Furthermore, since that time, the design points have been updated with improved Systems Code modeling. Understanding of the physics issues has evolved considerably since then as well, particularly with respect to the pedestal modeling and the interaction of the pedestal with the core.

The published ARIES-AT base configuration was reconstructed with the added H-mode pedestal, reproducing the equilibrium in Ref. [19]. A ONETWO calculation was performed to obtain profiles of current density, and bootstrap current using the published density and temperature profiles The GENRAY code was then used to simulate the LH current drive (LHCD) and ion cyclotron current drive (ICCD) required to make up the shortfall between the bootstrap and the total current density. This was compared with the published results that were obtained using the CURRAY code for the optimized L-mode configuration with two current drive scenario options. Table II and Fig. 4 show the comparison for the published Scenario 1 case in Ref. [19] with five wave spectra of LH

antenna grills, each centered at a different parallel wave number, $N_{//}$. It was found that the LHCD system can provide up to 0.63 MA for an axis electron density of $n_e \sim 3\times10^{20}$ m^{-3}. At higher densities than this, the LHCD efficiency was found to be much poorer.

The comparison with the previous published result shows lower LH current driven in the new calculations. This is probably due to the additional density pedestal in the new simulation; the edge was modified to include an H-mode edge density pedestal but the electron temperature T_e was set to be consistent with the *ad-hoc* H-mode equilibrium pressure profile. Thus, while internally consistent, the T_e profile is not that expected for H-mode confinement and both the edge density and temperature profiles are different from those in Ref. [19]. For the ICCD with frequency, $f = 96$ MHz, maximum $N_{//} = 2.0$, poloidal angle of the antenna grill $\theta = -15^\circ$, and power $P_{RF} = 4.7$ MW, the current driven was $I_{RF} = 0.11$ MA. This is also lower than that obtained previously, but probably for the same reasons as the smaller LHCD values. The differences between the GENRAY code results and the CURRAY calculations can be attributed to the new edge conditions. The next step, therefore, was to include a more self-consistent pedestal with both the temperature and density modified to be fully consistent with the equilibrium H-mode pressure pedestal obtained from the EPED1 model. This was then used as a new initial case for a steady-state scenario iteration, with heating and current drive optimized using the GLF23 transport model.

Table II
Calculated Current Drive Power Computed for the Lower Hybrid Current From the Simulation Using GENRAY for the 2006 ARIES Baseline and the Previously Published Results Using CURRAY. The New Results Also Use an Ad-Hoc H-mode Edge Whereas the CURRAY Simulations Used an L-mode Edge

			CURRAY (2006)		GENRAY (2011)	
Freq. (GHz)	**$N_{//}$**		**Power (37 MW)**	**I/P (A/W)**	**Power (37 MW)**	**I/P (A/W)**
3.6	1.65	-90	3.60	0.053	3.06	0.013
3.6	2.0	-90	4.40	0.049	4.40	0.020
3.6	2.5	-90	8.22	0.039	8.22	0.024
3.6	3.5	-90	8.87	0.024	8.87	0.021
2.5	5.0	-90	12.39	0.013	12.39	0.010

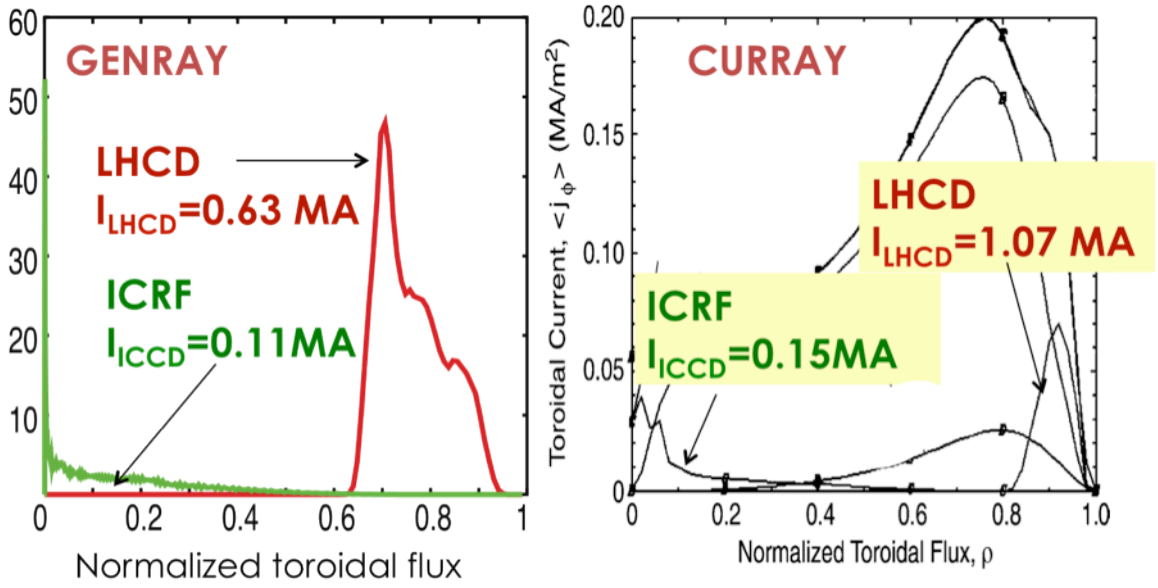

Fig. 4. Comparison of the LHCD and ICCD current drive profiles from the simulation for the 2006 ARIES simulation using GENRAY and the previously published results using CURRAY.

The EPED1 model prediction of the H-mode pedestal height and width for the 2006 ARIES baseline specifies a pedestal β_N of about 1.0 near $\rho = 0.93$. Here, ρ is the square root of the normalized toroidal flux. This pedestal was added to the published profiles and the equilibrium was recomputed and used as an initial profile in a ONETWO simulation. As in the previous benchmark simulation, this was iterated with a current-drive and transport simulation using the parallel ONETWO code coupled to GENRAY in order to align the profiles and iterate to obtain a self-consistent steady state scenario with heating and current drive optimized using the GLF23 transport model. For this purpose, the capability of launching multiple waves with different frequency from each launcher for LH or Fast Waves (FW) was added to the GENRAY code by including multiple grills in the poloidal plane. This is described briefly in Sec. 3.7 below.

Initial results from simulations using the GLF23 transport model with LH current drive provided by GENRAY show a steady state achieved after one full second of evolution with a pedestal β_N of 1.0. Results are shown in Fig. 5. The results shown are for fixed density and heating profiles, with the shifted circle geometry assumed by the GLF23 model.

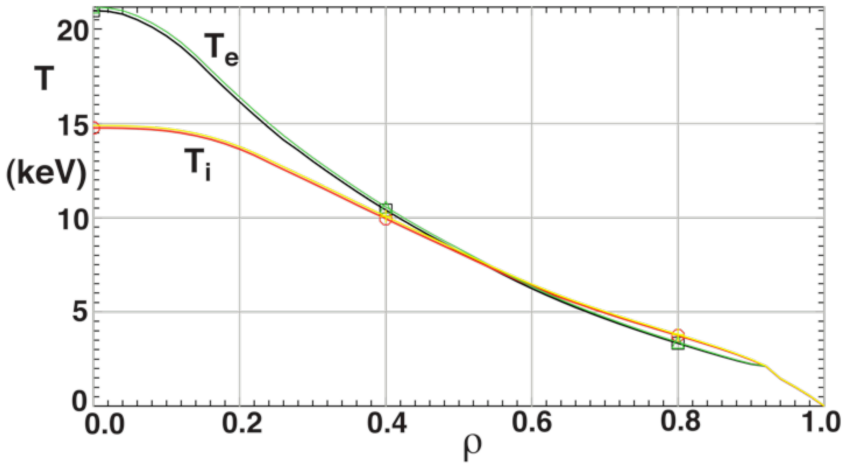

Fig. 5. Steady-state profiles of electron temperature T_e (black,green) and ion(red, yellow) electron temperature T_i obtained using the GLF23 transport model for the 2006 ARIES baseline with imposed pedestal. The green/yellow and red/black curves are due to different computational methods used. ρ is the normalized square root of the toroidal flux.

The more sophisticated TGLF model, which incorporates cross section shaping, is significantly more pessimistic. The same case run with the TGLF model did not reach a suitable steady state unless the boundary was moved in to about $\rho = 0.82$. Increasing the fusion heating power did not yield an improvement with TGLF. This therefore suggested that the original plan to utilize GLF23 in the initial steps of the optimization should be revisited and subsequent results discussed below confirmed this.

3.3. ACT 1A

From the Systems Code, an initial optimization for the advanced physics and advanced technology option resulted in a configuration with major radius $R_0 = 5.8$ m, aspect ratio $R_0/a = 4.15$, elongation $\kappa = 2.3$, and triangularity $\tau = 0.75$, with on-axis and line averaged electron densities $n_e = 1.95\times10^{20}$ m^{-3} and $\bar{n}_e = 1.61\times10^{20}$ m^{-3}, respectively, and axis electron temperature $T_e = 26.5$ keV. The corresponding ion axis density and temperature were slightly lower, with an impurity fraction resulting in $Z_{eff} = 1.27$.

This new ACT 1A scenario was substituted for the original 2006 base case but initially with no self consistent pedestal; instead, for this initial run, the pedestal boundary condition from the EPED1 prediction for the 2006 ARIES scenario was imposed. In contrast to the simulations for the 2006 baseline, the first simulations to find a steady state solution for the ACT 1A baseline using the GLF23 transport model found a complete profile collapse. This was attributed to a radiative collapse due to the large Argon impurity fraction imposed by the Systems Code to keep the heat flux to the divertor manageable. Consequently, the Ar fraction was reduced in the simulation to 10% of the original value, with a resulting $Z_{eff} \sim 1.2$. However, while this prevented the

complete collapse, the core region still partially collapsed, with the entire temperature profile reduced to the imposed boundary condition value set by the EPED1 model; this value, as noted, was derived for the previous ARIES scenario and is not completely consistent with the new ACT 1A equilibrium.

A steady-state was ultimately found with the density increased by a factor 1.85 in addition to the large Ar reduction. Figure 6 shows the rescaled density profiles used. This increase prevented the partial core collapse and the core electron heat flux was found to be at approximately neoclassical levels, with the ion heat fluxes somewhat larger. The initial and final steady state density and temperature profiles are shown in Fig. 6. There is still a partial radiative collapse outside the core to values significantly below the initial temperatures since the mid range and edge region steady state temperatures are essentially held at the imposed boundary condition value, as seen in Fig. 7. Analysis of the time dependent simulation shows that a transport barrier in the electron temperature forms initially but subsequently decays. This is also shown in Fig. 7. It is also ofs

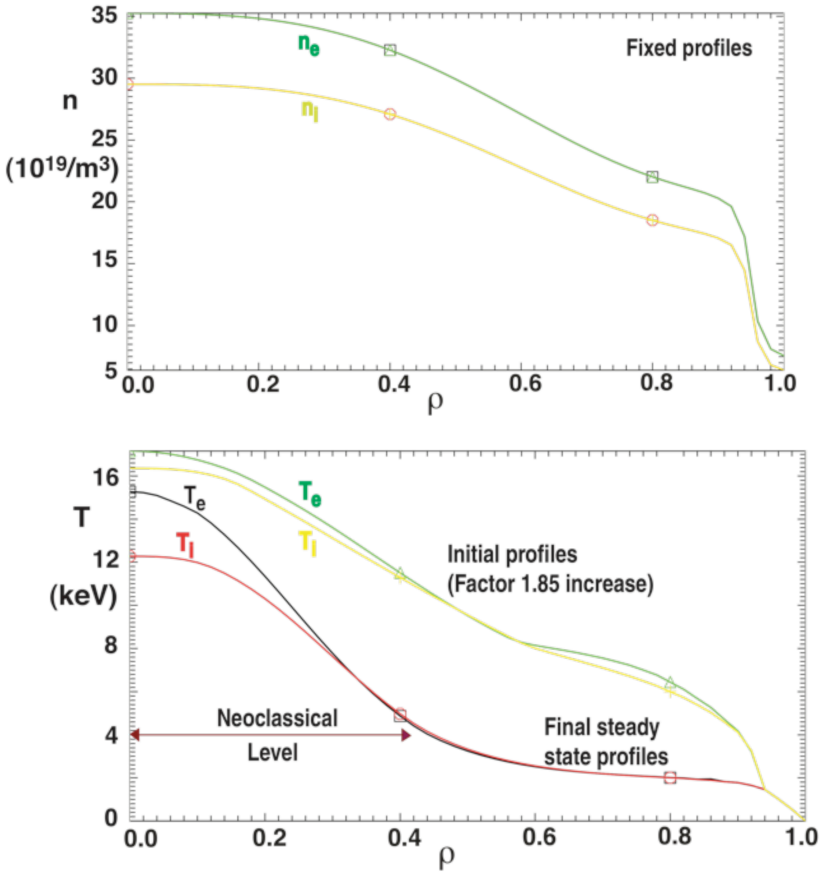

Fig. 6. (a) Fixed density profiles used in the ACT 1A simulation with axis density scaled up by a factor 1.85 and Ar fraction reduced to 10% below the Systems Code values. (b) Steady-state temperature profiles obtained. ρ is the normalized square root of the toroidal flux.

interest that the profiles do not actually evolve to a strict steady state and instead, the simulations show small long-term oscillations. This is often seen in other simulations but the oscillations are small enough that they would have no practical consequences.

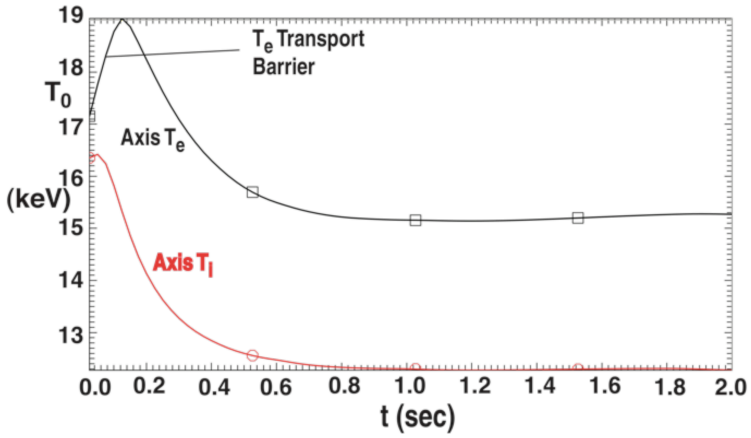

Fig. 7. Time evolution of the electron and ion axis temperature values evolving to steady state in the ACT 1A simulations, showing the initial T_e transport barrier formation, manifested as a sharp inrease in the axis T_e value, and subsequent decay, and the small long-term oscillations.

Figure 8 shows the diagnosis of the individual species heat fluxes from the initial state and the final steady state. These show a large flux initially as the arbitrarily imposed profiles adjust and evolve toward a steady state with much reduced heat fluxes. The initial steep gradient at the edge is an artifact of the imposed boundary condition. In steady state, the fluxes have adjusted to be compatible with the set boundary condition.

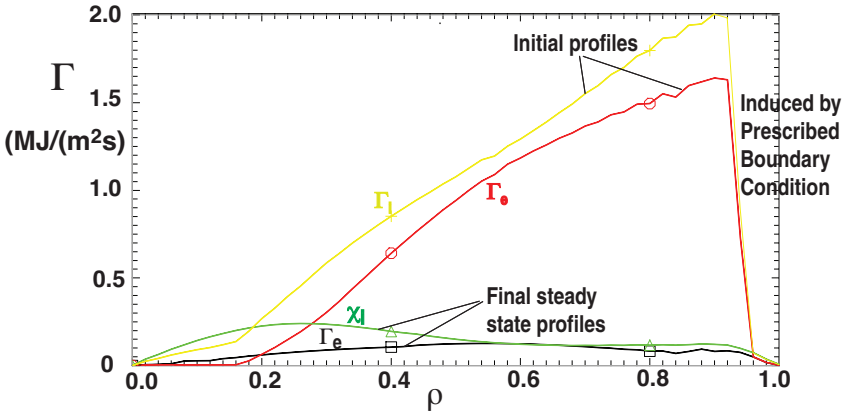

Fig. 8. Initial and final steady-state heat fluxes versus toroidal flux for ACT 1A showing the large reduction from the initial transient fluxes in the final values once a quasi-equilibrium steady state is established. ρ is the normalized square root of the toroidal flux.

Sensitivity studies found that the density factor increase where a steady state solution can be achieved has a small range between 1.8 and 1.9; lower values lead to a partial

collapse of the whole profile, and larger values lead to runaway core peaking from formation of an internal transport barrier.

Subsequent work turned to analysis of a new updated design with updated profiles and boundary called ACT 1B. This is described in the following subsection. The same issues of profile collapse appeared, however, in the ACT 1B scenario. Further diagnosis of the issue in this case led to a change in the original simulation plans, as will be described.

3.4. GLF23 Simulations for ACT 1B

The ACT 1B baseline had enough significant changes to require that the simulations be repeated. The first step necessary was to construct a new force balance equilibrium required by the ONETWO simulation since the new profiles were obtained directly from a JSOLVER inverse equilibrium, which does not include a divertor, but the updated boundary, which does include the divertor, was obtained from a direct equilibrium calculation using the TSC code. A new code was written to take these inputs and construct an initial guess for the EFIT equilibrium code and from this the new equilibrium was constructed. A new Greens Function table for the coils and vacuum fields was constructed for the modified geometrical configuration.

A pedestal was then imposed that is fully consistent with peeling-ballooning stability for this initial equilibrium, using the EPED1 model to provide the edge pedestal height and width and the pedestal poloidal beta value β_N^{ped}. It was hoped that this might also solve some of the profile collapse issues encountered in the ACT 1A scenario. The equilibrium was updated to include this.

The EPED1 pedestal model value for β_N^{ped} is used as a boundary condition for the transport simulations; the transport simulations are well known to be inaccurate in and beyond the pedestal in H-mode and therefore require the boundary condition to be imposed at a point interior to the pedestal. The position for imposing this boundary condition was chosen to be at $\rho = 0.93$, which is at the top of the pedestal. The results indicate that β_N^{ped} values in the range $1 < \beta_N^{ped} < 1.1$ at $\rho \sim 0.9$ provide reasonable solutions. The value $\beta_N^{ped} = 1$ was chosen for the simulations.

The self-consistent transport simulation was run for this equilibrium to determine if the same issues of collapse as in the ACT 1A scenario ensue. Plans for these simulations were revised slightly from the original. Most notably, it was realized that the transport simulations require some additional sensitivity studies with respect to the density in order to understand the collapse when the density is too low. Subsequent steps then followed

the overall plan of running a self-consistent steady state scenario iteration with heating and current drive optimization using GENRAY and the GLF23 transport model.

Transport simulations were performed for model profiles with broad density inside the pedestal region, parameterized using a cubic spline. The ion density at the pedestal is determined by given value of β_N^{ped} from the EPED1 modeling. The temperatures were derived initially from the equilibrium pressure and the prescribed density for the individual species assuming $Z_{eff} = 1.27$ and $T_e = T_i$. The temperatures were subsequently evolved using the GLF23 transport model assuming no density evolution and no auxiliary heating so that the only energy source to maintain the temperatures was alpha particle heating. The temperatures were held fixed at $\rho = 0.93$ as the boundary condition. The density is not evolved in these simulations; essentially it is assumed that they are maintained against particle diffusion by a source.

Figure 9 shows the density and temperature profiles for the ions and electrons. For this case, the final steady state found was non-burning as the profiles ultimately collapsed to the boundary condition value, similar to the results using the *ad-hoc* pedestal model in the ACT 1A simulations. Thus, the slightly inconsistent pedestal in the ACT 1A simulations was not the major cause of the collapse. Essentially, the fusion alpha particle heating could not be maintained against the predicted outward heat flux. The final collapsed profiles are shown in Fig. 9(b).

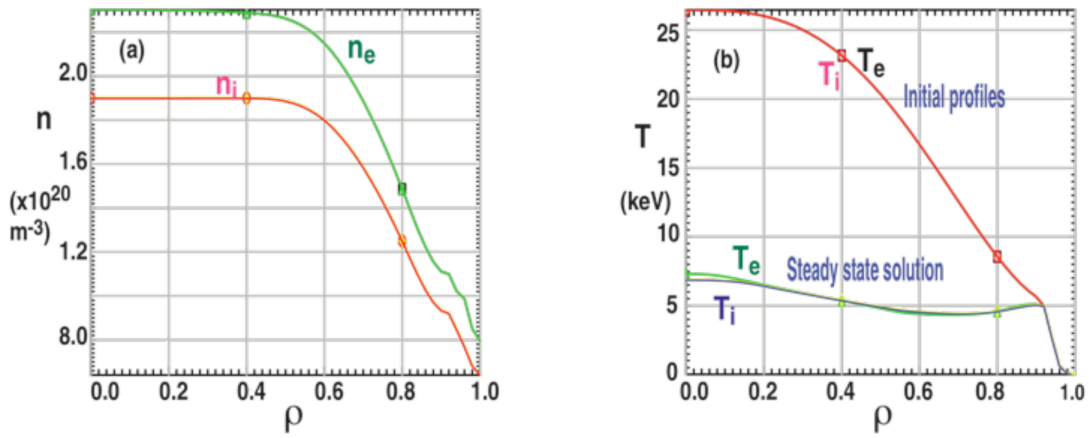

Fig. 9. Standard ACT 1B case ion and electron (a) density and (b) temperature profiles. In (b) the final collapsed steady state is also shown. ρ is the normalized square root of the toroidal flux.

Two scans in the density were performed, one scan with flat density profiles as in the standard case, and one for peaked density profiles, each with varying axis values. Figure 10(a–d) show the profiles of density and temperature for the flat density case with the three different values of the axis value. The standard case in Fig. 9 is the lowest density case of this series. Transport simulations evolving the temperatures were again

performed for each density profile and axis value. Figure 11 shows the corresponding evolution of the central electron and ion temperatures. After an initial transient increase corresponding to the formation of a core electron transport barrier and a weak ion transport barrier, the two profiles with the lowest density eventually collapse but the highest density case appears to reach a steady state with elevated temperature and sustained fusion. This value for the axis density is 80% higher than the Systems Code value, similar to the ACT 1A results.

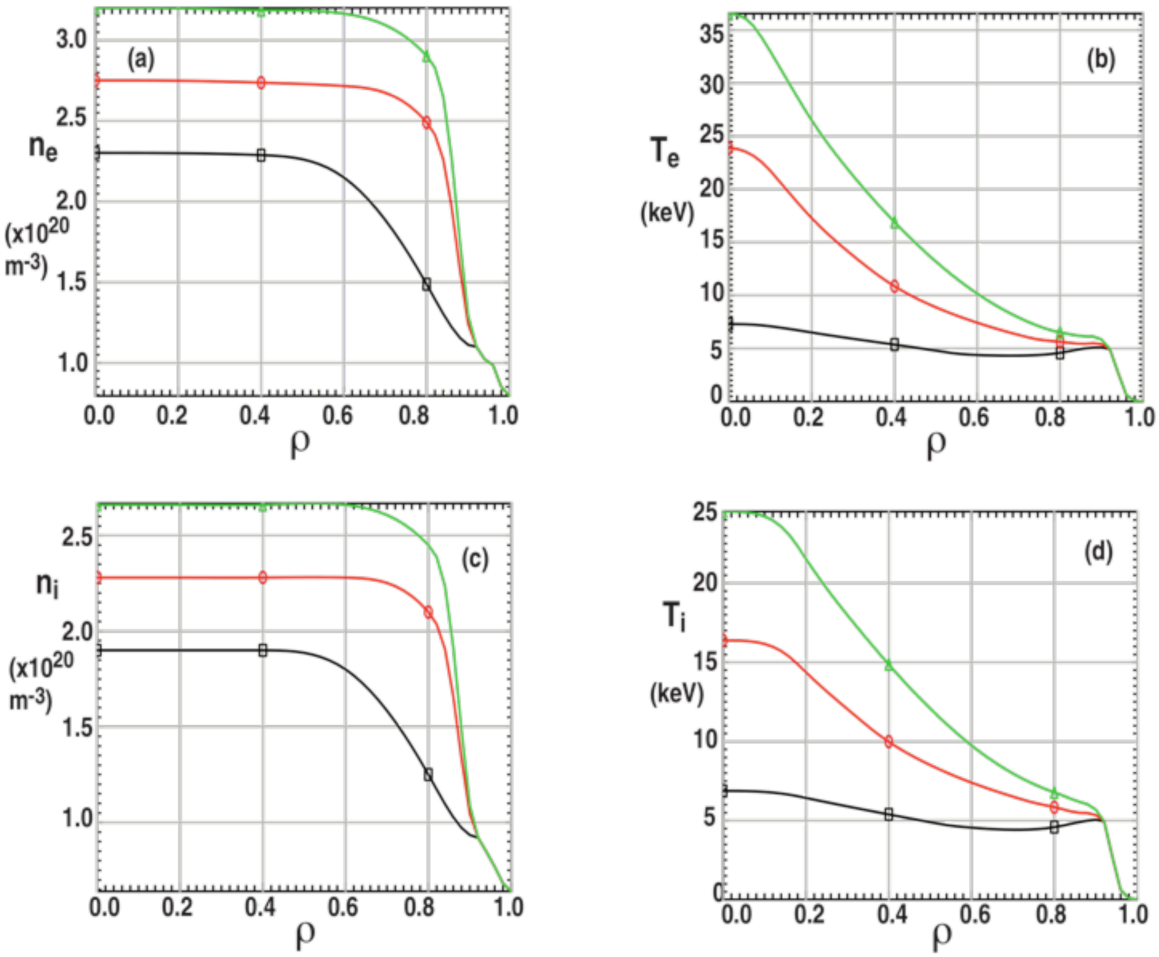

Fig. 10. Flat density case electron (a) density and (b) temperature profiles and ion (c) density and (d) temperature profiles for the three chosen axis density values in the GLF23 simulations for ACT 1B. ρ is the normalized square root of the toroidal flux.

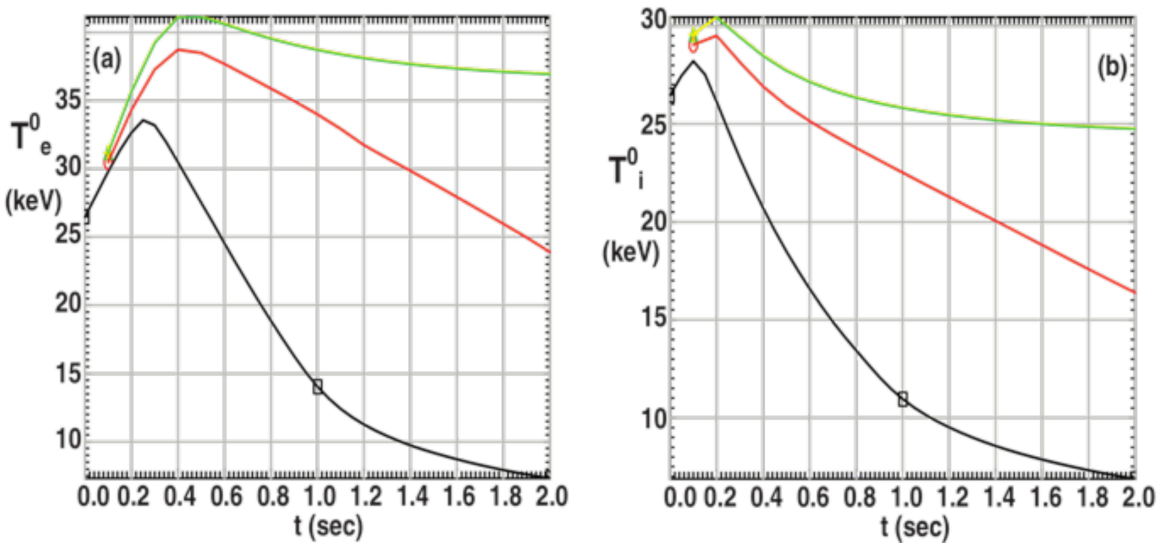

Fig. 11. Axis temperature evolution for the flat density cases of Fig. 10 showing (a) electron and (b) ion temperature.

It is widely believed that peaking of the density increases fusion power since in the core, where the ion temperatures are above the threshold for fusion, fusion power is proportional to density. However, the gain for this case is weak. Figures 12(a–d) show the profiles of density and temperature for the peaked density scan, again with three values for the density on axis, and Fig. 13 shows the corresponding time evolution of the axis temperatures. The collapse for the intermediate density case is partially arrested but the simulation was not run for enough time to confirm whether a true steady state is sustained. Otherwise, despite the conventional expectation, there appears to be little gain from peaking the density profile in this case. Again, a transport barrier appears transiently but is somewhat weaker than for the broad density scan.

To better understand the effect of peaking of the density profile, the moderately peaked density profile in Fig. 12 with increased density was compared with a case with stronger core peaking. Figure 14(a) shows the electron and ion density profiles for the two cases. The electron and ion energy fluxes computed from the GLF23 model are shown in Fig. 14(b). In both cases, the outward energy flux is large in the outer region $0.6 < \rho < 0.8$. However, the additional density peaking results in an additional large energy flow in the region of the additional peaking, $0.2 < \rho < 0.4$. Thus, additional core peaking beyond that in Figs 12 and 13 is not beneficial.

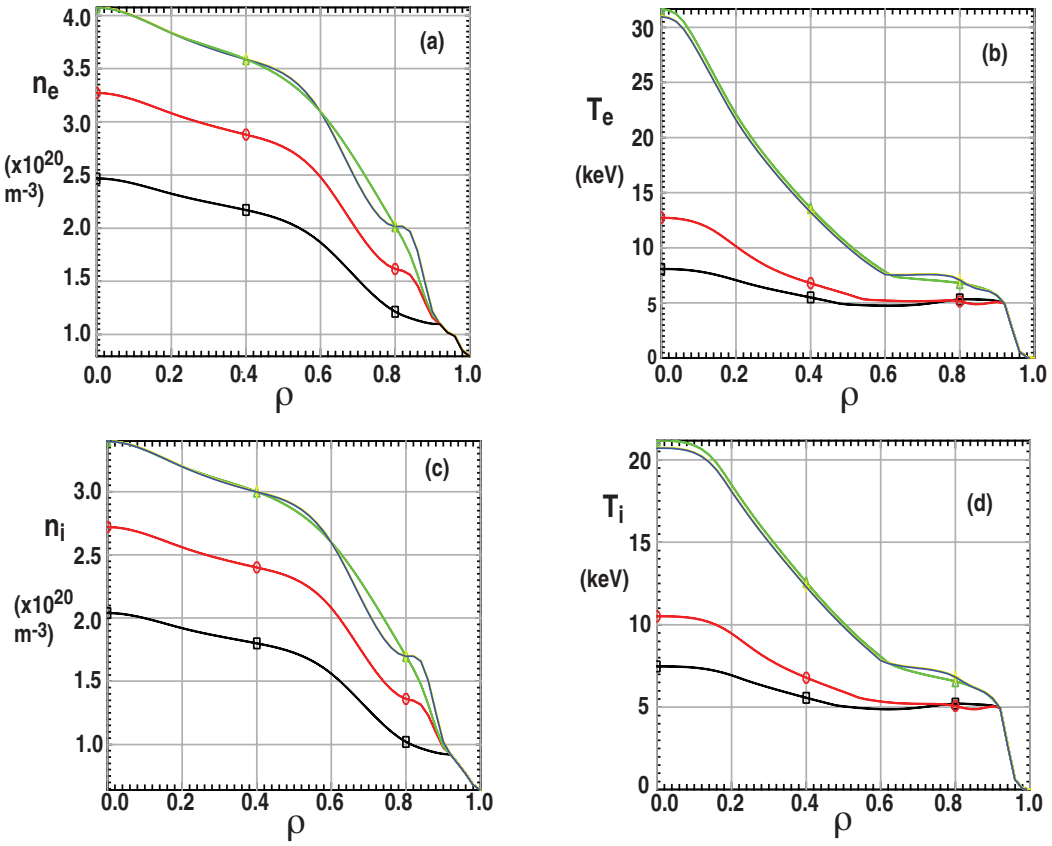

Fig. 12. Peaked density case electron (a) density and (b) temperature profiles and ion (c) density and (d) temperature profiles for the three chosen axis density values in the GLF23 simulations for ACT 1B. ρ is the normalized square root of the toroidal flux.

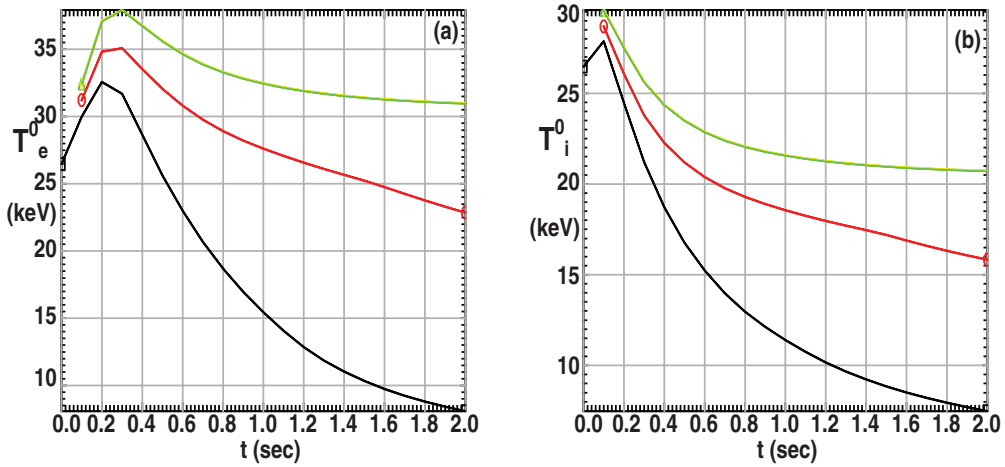

Fig. 13. Axis temperature evolution for the peaked density cases of Fig. 12 showing (a) electron and (b) ion temperature.

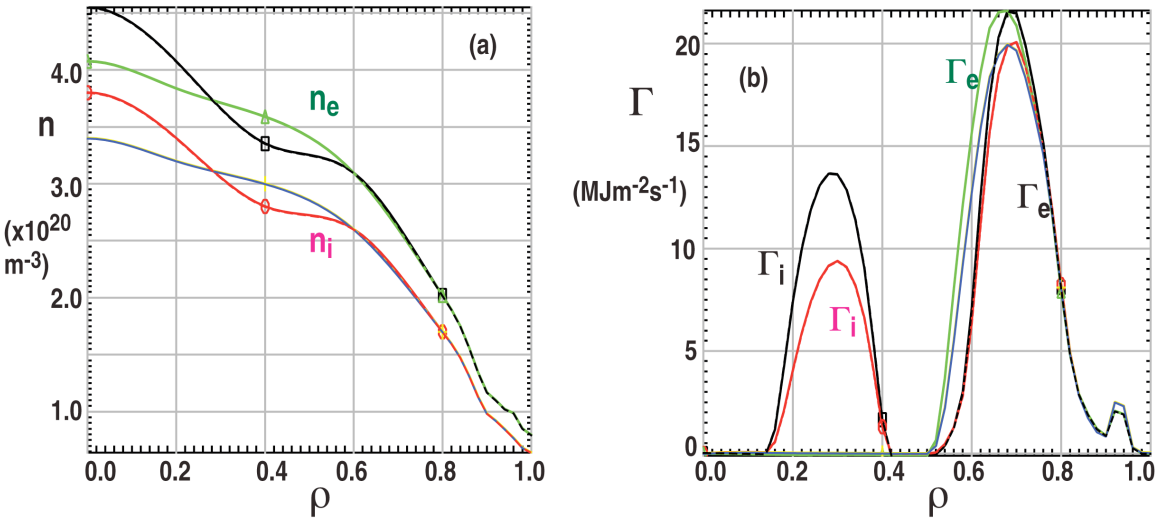

Fig. 14. Comparison of (a) elecron and ion density profiles with and without central peaking and (b) analysis of the individual electron and ion heat fluxes for the ACT 1B simulation using GLF23. ρ is the normalized square root of the toroidal flux.

With respect to the current drive required to sustain the q profile, a large bootstrap in the pedestal region results in an overdrive of the plasma current there. For the broad density cases, the residual Ohmic current is large and negative everywhere and FW current drive (FWCD) near the axis is not feasible. For the peaked density case, overdrive is reduced substantially but the bootstrap current yields insufficient current density near the axis and additional current drive on axis is needed to reduce the inductive Ohmic current to an acceptable level close to zero. About 40 MW of FW is able to drive the 50A on axis needed and good alignment of the total current with bootstrap current seems possible for the more peaked density profiles. Including 1.05 MW of FWCD and LHCD, the residual Ohmic current in steady state is 600 kA. Further optimization should reduce this even further.

The transport simulations performed for flat and peaked density model profiles in the ACT 1B configuration confirm that without additional auxiliary heating, the profiles using the Systems Code optimized on-axis density cannot be sustained according to the GLF23 model and that the density needs to be increased by almost a factor of two. Several attempts were made to resolve the profile collapse. First, the simulations were repeated with an additional 40MW heating in addition to the current drive to see if the temperature collapse can be prevented without raising the density. However, as was expected, this made essentially no difference since the dominant heating should come from self heating from the fusion reactions. The density was still needed to be increased by 80% to avoid a collapse of the profiles.

Calculations were also performed to test the sensitivity to the location of the pedestal boundary condition ρ_b since the analysis of the outward energy flux in the moderately peaked density case but with increased magnitude shows that it is concentrated at $0.6 < \rho < 0.8$. These found that the collapse could be avoided if the boundary condition is applied well inside the pedestal region, confirming that the collapse results from excessive energy transport in the outer regions; essentially moving the boundary condition further inside eliminates any transport outside. This is shown in Fig. 15. For $\rho_b > 0.8$ the profiles collapse, corresponding to large energy fluxes in the outer region. When ρ_b is moved inside the peak outward flux at $\rho_b \sim 0.7$, however, enough outward flux is artificially eliminated from the computation that the profiles can be sustained.

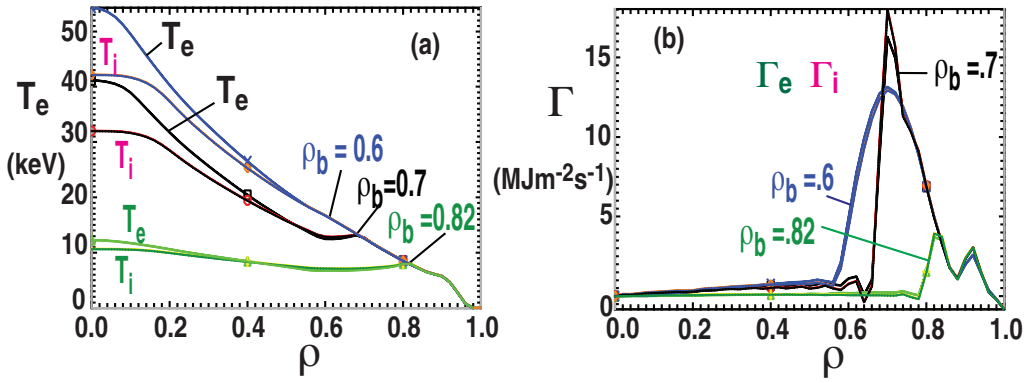

Fig. 15. Variation with position where the boundary condition is applied of (a) the final steady state electron and ion temperature profiles and (b) the electron and ion energy fluxes, for the ACT 1B simulation. ρ is the normalized square root of the toroidal flux.

3.5. Full Geometry Transport Simulations for ACT 1B

The solution was tested using the more sophisticated and more realistic, but much more computationally expensive TGLF transport model to determine if there are large differences from the simplified GLF23 predictions. The TGLF code includes real shaped geometry in addition to using a set of twice as many basis modes in constructing the microinstabilities [20]. As in the simulations for the 2006 design, it was expected that TGLF would yield more pessimistic predictions than using GLF23. However, because the densities were not evolved in this study, the GLF23 electron ion dynamics due to density gradients is an invariant of the simulations. In that case, GLF23 can be overly pessimistic. In fact, for this case, the results were uncharacteristically more optimistic than the GLF23 simulations and sustained steady state solutions were found. The profile was, however, modified slightly with additional peaking to avoid a collapse. In addition, in this simulation, the density profile was evolved with the temperatures for some time and then fixed only later in the evolution; this fixing of the density avoids numerical stability problems. However, because the density evolves, β_N^{ped} is no longer fixed at the

EPED1 determined value of 1.0, some further iteration will be needed to maintain consistency with this pedestal condition.

The final steady state profiles for the density and temperature of the two species are shown in Fig. 16. This scenario from the TGLF simulation, with slight additional density peaking but without needing to otherwise increase the density profile yields a fusion power of P_{DT} = 740 MW. While too low, further optimization should improve this value.

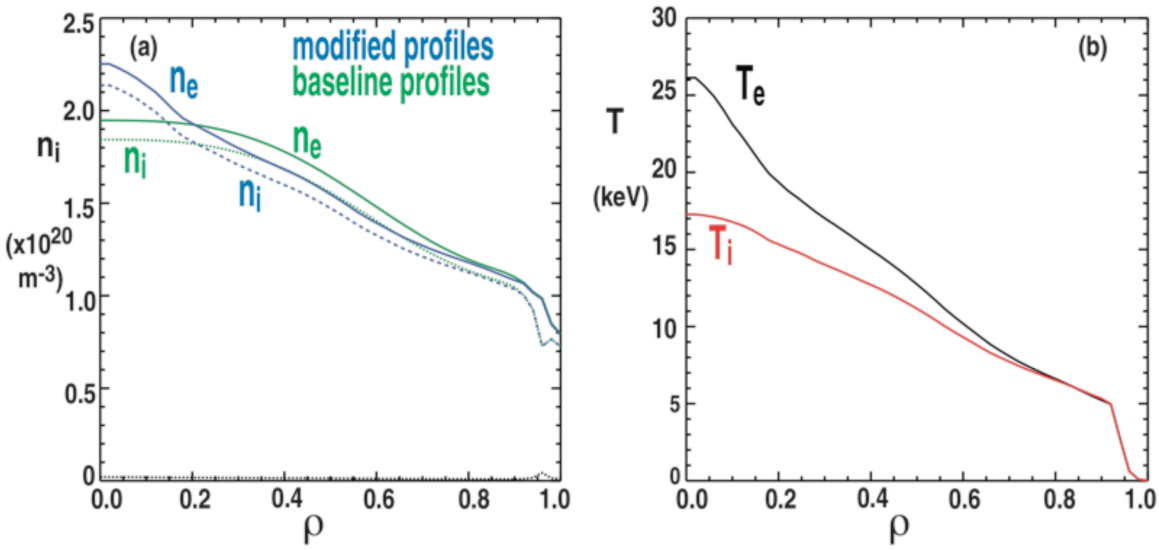

Fig. 16. Simulation results for ACT 1B from TGLF with slightly peaked density profiles (a) electron and ion density profiles, and (b) electron and ion temperature profiles. Shown also in (a) are the baseline density profiles for comparison. ρ is the normalized square root of the toroidal flux.

It is clear that the GLF23 simulations are quite misleading in these cases. However, the more sophisticated TGLF simulations are prohibitively time consuming for routine simulations. It was decided therefore that future work will invoke instead the Multi-Mode Gyrofluid transport model [23]. The Multi-Mode model was accordingly successfully implemented in the parallel version of the ONETWO transport code. The Multi-Mode code claims to have similar predictive capability as the TGLF model but to be much faster and therefore more suitable for the simulations being done here. While the Multi-Mode model is approximately ten times slower than the simple GLF23 model, it includes full geometry and is ten times faster than the full geometry TGLF model. The model includes the Weiland model for the TEMs and ion temperature gradient (ITG) driven modes as the dominant contributions for electrons and ions respectively. Additionally, drift ballooning modes (DBM) are included.

The first iteration from the ACT 1B initial state found reasonable steady state solutions with no collapse in the profiles. The electron and ion species temperatures were

initialized with $T_e = T_i$ and then evolved to steady state using the computed Multi-Mode model transport coefficients for both species. In contrast to the TGLF simulations, the density profiles were fixed in time. The temperatures were evolved to steady state where the residual electric field was small and of the order of a millivolt for both cases without collapse.

Two cases were considered with different line averaged density: for $n_e = 1.67 \times 10^{20}\ \mathrm{m}^{-3}$, a steady state fusion power of $P_{DT} = 1.1\,\mathrm{GW}$ and $Q_{DT} = 28.7$ was obtained. For a slightly higher density case, obtained by varying the profile broadness with the axis density kept fixed at the standard value, the line averaged density was $n_e = 1.78 \times 10^{20}\ \mathrm{m}^{-3}$, and $P_{DT} = 1.5\,\mathrm{GW}$ and $Q_{DT} = 39.7$. Figure 17 shows the density profiles in the two cases.

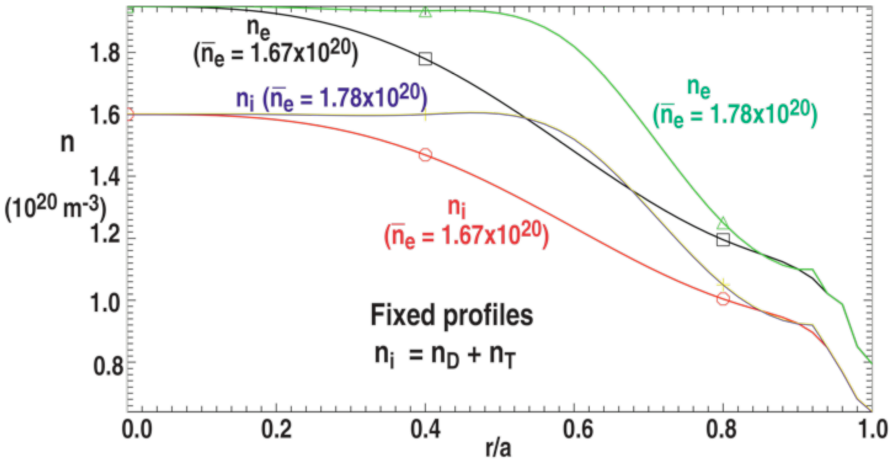

Figure 17. Electron and ion density profiles used in the ACT 1B simulations. r/a is a radial variable equal to the normalized square root of the toroidal flux.

Comparison of the electron and ion steady state fluxes with those obtained using the GLF23 transport model in Fig. 18 shows clearly that the Multi-Mode model has a much reduced flux in the outer region. Both species fluxes are reduced by almost an order of magnitude over the GLF23 fluxes outside $r/a = 0.6$.

Electron transport in the GLF23 simulations showed an apparent large TEM contribution; although GLF23 does not identify the individual contributions, the TEM is believed to be the dominant non-Electron Temperature Gradient (ETG) contribution. In contrast, diagnosis of the transport shows the ETG as the dominant electron transport mechanism in the Multi-Mode model. This is shown in Fig. 19(a). The TEM contribution, which is included in the Weiland electron transport model that is part of Multi-Mode, is smaller than but is still comparable to the ETG transport.

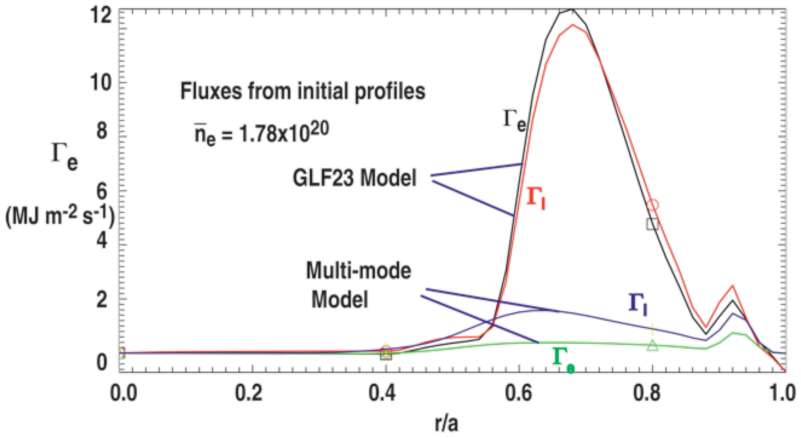

Fig. 18. Comparison of transport flux predictions between GLF23 and Multi-Mode for the ACT 1B simulations. r/a is a radial variable equal to the normalized square root of the toroidal flux.

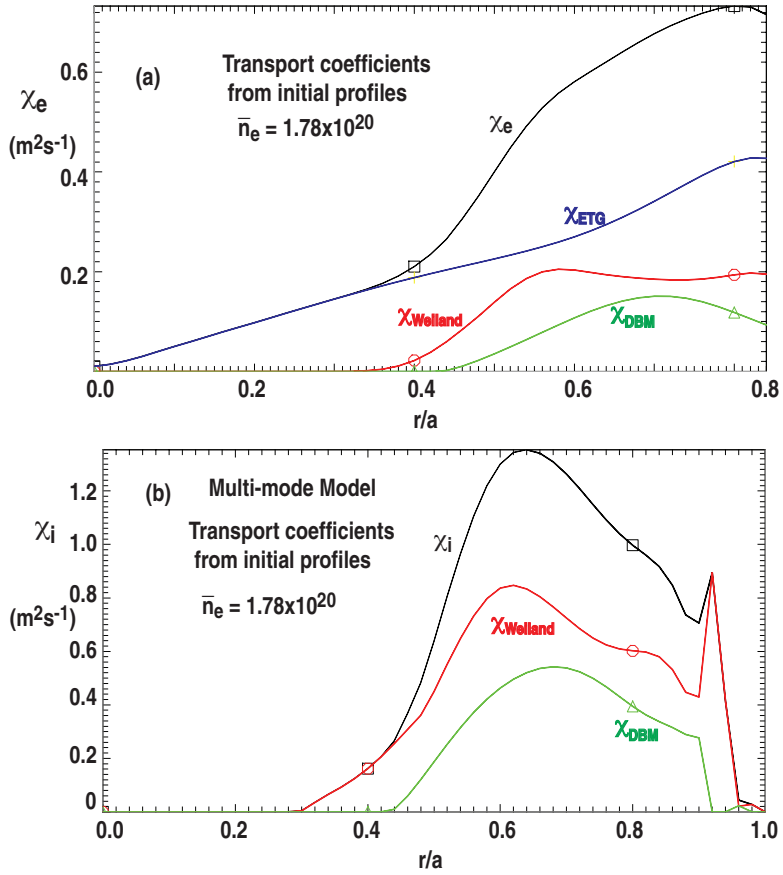

Fig. 19. Transport flux contributions in Multi-Mode simulations for the ACT 1B case with line averaged density $n_e = 1.78\text{x}10^{20}$ m^{-3} (a) electrons and (b) ions. r/a is a radial variable equal to the normalized square root of the toroidal flux.

Diagnosis of the ion transport shows ITG modes, also contained in the Weiland model, is the largest contribution. DBMs are also significant; these are not included in either the GLF23 or TGLF models. Figure 19(b) shows the steady state ion transport contributions from the various modes for the $n_e = 1.78 \times 10^{20}$ m^{-3} case.

The major issue in this simulation is the considerable evolution of the q profile before reaching the steady state. In particular, the axis temperature overheats causing a large on-axis current density despite the small residual steady-state electric field. Figure 20 shows the time development of the axis electron and ion temperatures for the two density values. The steady state electron temperatures remain above 40 keV while profile integrity is maintained out to the edge boundary condition where it is fixed. This is shown in Fig. 21. There is a slight mismatch where the edge boundary condition is applied that should be eliminated on further iterations.

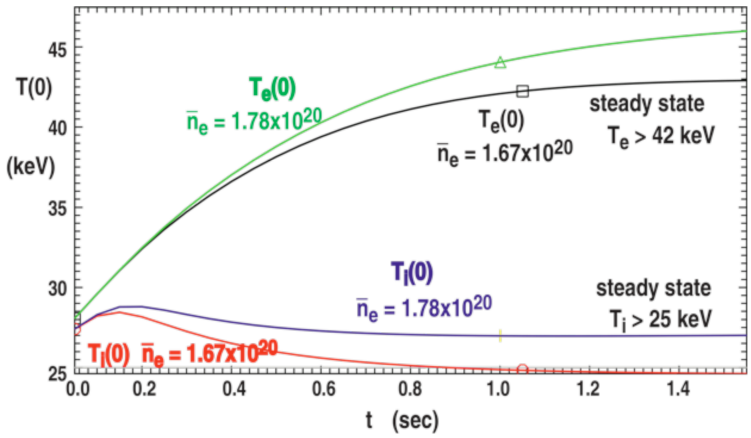

Fig. 20. Axis temperature evolution for ACT 1B using the Multi-Mode transport model showing evolution to steady state with $T_e > 42$ keV and $T_i > 25$ keV.

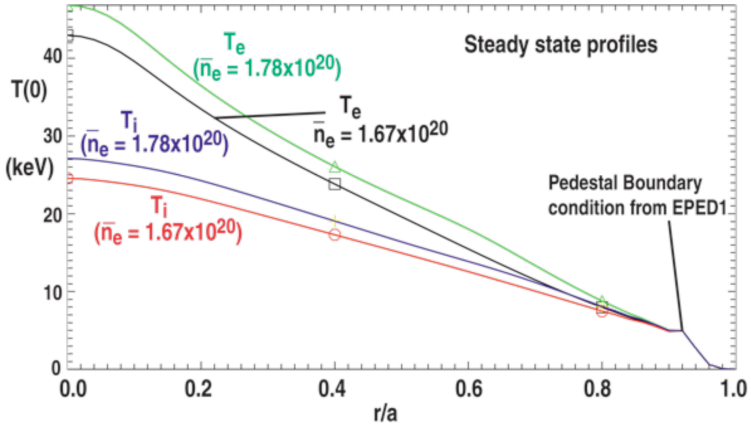

Fig. 21. Final steady state temperature profiles evolution for ACT 1B using the Multi-Mode transport model. r/a is a radial variable equal to the normalized square root of the toroidal flux.

The excessive axis electron temperatures create issues with the viability of the final state. Of particular importance, the safety factor on axis, q_0 , evolves to a value well below unity even with only a small residual electric field and the final state is probably strictly unstable. The high axis T_e implies that the local current density can still be large since $j \sim E_0/\eta \sim E_0 T_e^{3/2}$. The initial profiles have $q_0 \sim 3$ but evolve to $q_0 \sim 0.95$ for $n_e = 1.78\times10^{20}$ m^{-3} and to $q_0 < 0.5$ for . This is likely to be unstable to internal kink modes in both cases, with the instability usually manifested as a periodic sawtooth. While sawteeth can be tolerated, the performance is expected to significantly reduced.

A large local externally driven current is required to eliminate the Ohmic current density on axis. For the $n_e = 1.67\times10^{20}$ m^{-3} case, the breakdown for the bootstrap, residual Ohmic, and RF contributions is $I_{boot} = 4.9$ MA, $I_{Ohm} = 3.1$ MA, and $I_{RF} = 2.6$ MA respectively. For the $n_e = 1.78\times10^{20}$ m^{-3} case, the corresponding contributions are $I_{boot} = 6.6$ MA, $I_{Ohm} = 1.4$ MA, and $I_{RF} = 2.5$ MA. Figure 22 shows the profiles of the contributions for the two different line averaged density simulations. In future simulations, the intent is to eliminate the overheating and excess axis current density by small changes in the initial profile and then evolve this to a steady state with $q_0 > 1$.

Subsequently, a new design iteration with increased size from the Systems Code was adopted by the ARIES group. While most of the lessons learned from the ACT 1A and ACT 1B design points were transferred and applied immediately to these simulations — specifically the use of the Multi-Mode transport code, the new design presented additional challenges that first needed to be overcome.

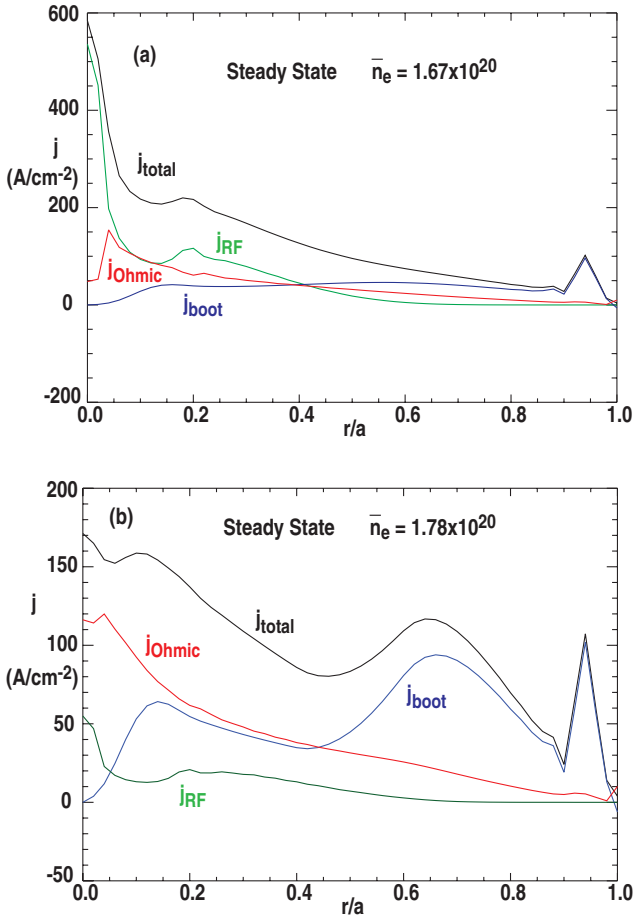

Figure 22. Steady-state current density contributions in the Multi-Mode transport simulations (a) $1.67x10^{20}$ m^{-3} and (b) $1.78x10^{20}m^{-3}$. r/a is a radial variable equal to the normalized square root of the toroidal flux.

3.6. ACT 1 Final Design

The major radius of the ACT 1 design was increased from $R_0 = 5.8$ m to $R_0 = 6.75$ m but with constant aspect ratio. The change was sufficiently large that it required a new starting equilibrium from the TSC code. The convergence of the new TSC equilibrium was quite poor but preliminary self consistent transport and current drive simulations were initiated using a slightly modified version of the TSC equilibrium; in addition to remapping the equilibrium file to standard format, the modification simply reconstructed the pressure and toroidal field function to be more consistent with their derivatives that define force balance.

A preliminary extrapolation to a state with zero electric field was calculated by solving the transport equations with time derivatives set to zero. This simulation found a

much reduced plasma volume and final steady state profiles that are very different from the initial profiles. The comparison of the initial equilibrium with the steady state extrapolation is shown in Fig. 23, with (a) the initial profiles and (b) the final profiles extrapolated to steady state. This large difference suggests that the initial profiles are probably too far from steady state to develop to a steady state solution. However, the equilibrium is sufficient for current drive calculations and preliminary results suggested that a combination of LH and a small amount of FW on axis is sufficient to maintain the final steady state profiles.

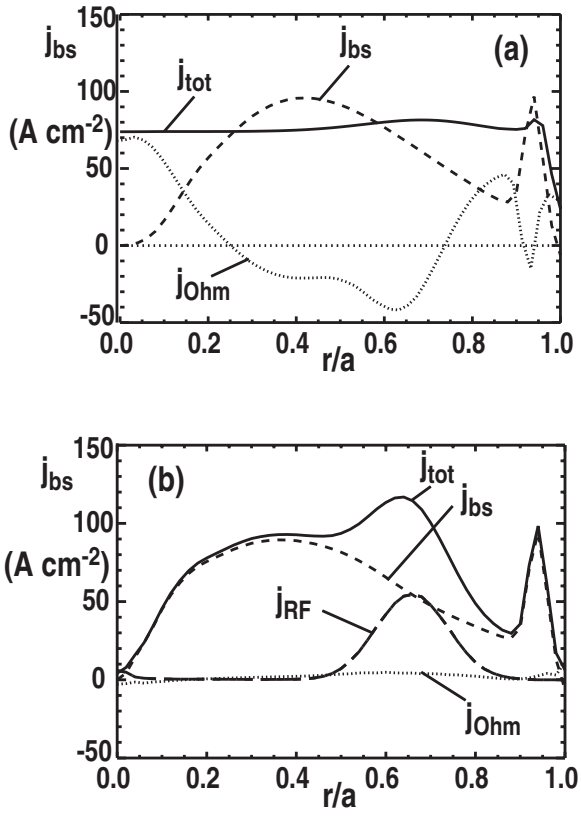

Fig. 23. Comparison of initial equilibrium with steady state extrapolation for the final ACT 1 design point. (a) Initial profiles. (b) Final extrapolated steady-state profiles. r/a is a radial variable equal to the normalized square root of the toroidal flux.

Nevertheless, the poor convergence of the TSC equilibrium obtained resulted in problems for the transport evolution and ultimately required reconstruction of a new equilibrium using EFIT. The new larger major radius configuration required a new Greens function table describing the vacuum field from the new coil positions. The new table was constructed but the equilibrium failed to converge from the remapped TSC equilibrium taken as an initial guess. Superficially, there appeared to be insufficient vertical field provided from the new coils to close the surfaces.

The issues were finally resolved after considerable work. The equilibrium that was originally provided from the TSC code had profiles that were not consistent with the specified total current and provided approximately only half the needed current. Consequently, the profiles were rescaled to reproduce the correct total integrated current and the equilibrium force balance was recomputed. A pedestal pressure consistent with EPED1 from the ACT 1B simulations was imposed; this appeared to be sufficient given the insensitivity of the EPED1 results to fairly wide equilibrium variations. This equilibrium was used in the subsequent simulations.

The initial transport simulations using this new design and the Multi-Mode model produced a steady state solution but with low fusion power and further optimization will be needed to raise this. The density profile shape was found to be crucial to obtaining reasonable performance parameters using only fusion heating. The configuration is shown in Fig. 24. This shows the initial equilibrium obtained from TSC (black) overlaid with the initial free boundary equilibrium obtained from EFIT (red) using the ACT 1 coils prescribed from the TSC code and the fixed boundary version (blue) obtained by resolving the equilibrium but with the boundary fixed in order to obtain sufficiently tight convergence. The corresponding equilibrium pressure profiles are shown in Fig. 25. Figure 26 shows the density and temperature profiles used in the transport simulations. Here, in (a), the initial density profiles were fixed in the simulation as the temperature were evolved using the Multi-Mode model, with the final steady state temperatures shown in Fig. 26(b).

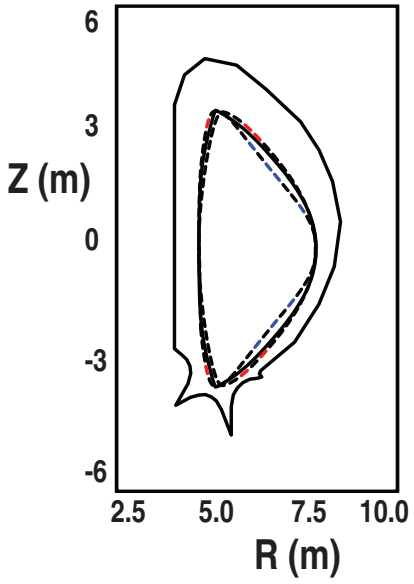

Fig. 24. Reconstructed final ACT 1 design point equilibria showing the initial TSC equilibrium (black) overlaid with the EFIT generated free boundary equilibrium (red) and the fixed boundary equilibrium (blue).

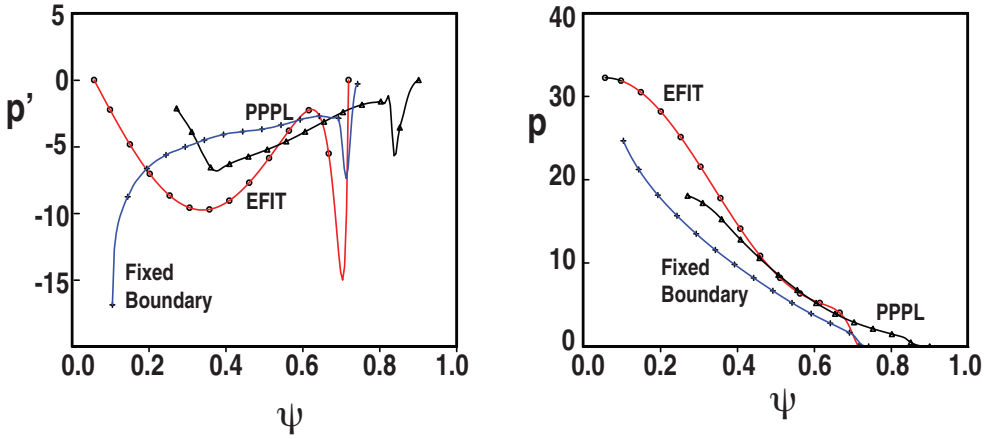

Fig. 25. Reconstructed final ACT 1 design pressure profiles showing the initial TSC equilibrium with the EFIT generated free boundary and fixed boundary equilibria. ψ is the normalized poloidal flux.

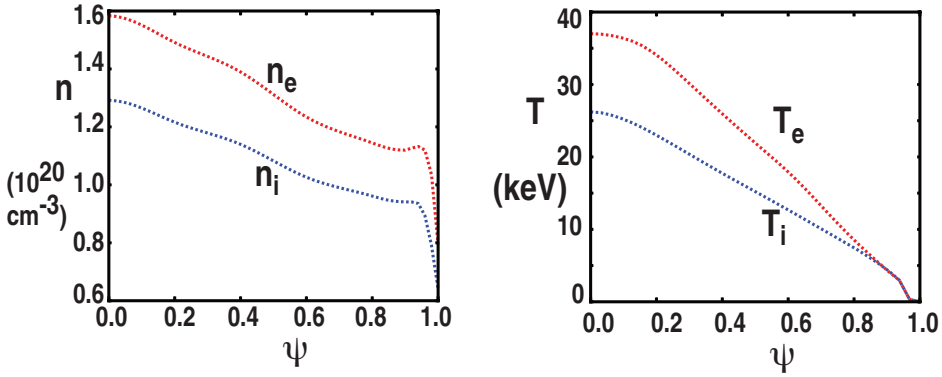

Fig. 26. Profiles for the final ACT 1 scenario (a) initial density and (b) steady state temperatures. ψ is the normalized poloidal flux.

An analysis of the individual energy transport mechanisms was also carried out and the results are shown in Fig. 27. Here, the contrubtions from the Weiland model and the DBM mechanisms are shown for both species and the ETG contribution for electrons are shown. The TEMs and ITG modes are respectively the dominant contributions for electrons and ions in the Weiland model. The DBM and Weiland model mechanisms contribute roughly equally and to both electron and ion transport. The ETG modes, however, are predicted to be the dominant energy transport mechanism for the electrons.

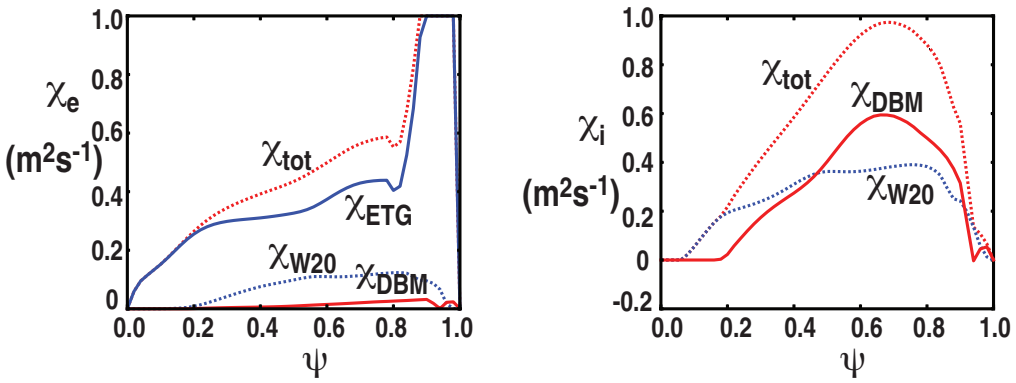

Fig. 27. Analysis of the individual energy transport mechanisms from the Multimode model. ψ is the normalized poloidal flux.

The current drive mix required to sustain the steady state is shown in Fig. 28(a) and the final q profile is shown in Fig. 28(b). The major result to note here is that the bootstrap current contributes almost all of the current, with the Ohmic contribution essentially negligible and the external current drive contributions small. The 200 MHz FW contribution requires 1.5 MW and the 5 GHz LH requires 1 MW.

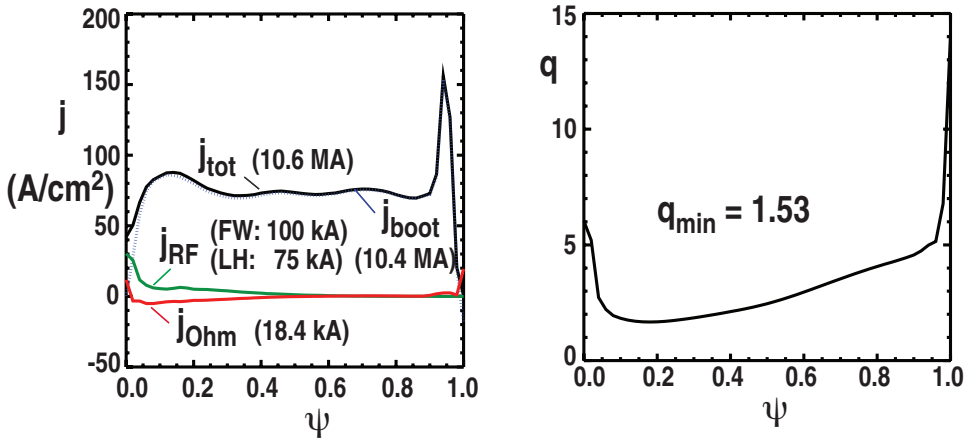

Fig. 28. Breakdown of current drive contributions required to sustain the steady state for the final ACT 1 scenario. ψ is the normalized poloidal flux.

The configuration obtained in steady state differs somewhat from the initial state and further iteration is necessary to obtain a fully self consistent solution. As a result of the funding reductions, however, this was not done.

3.7. Code Development

In addition to the major coding effort to incorporate the Multi-Mode transport model into the parallel version of the transport simulation code ONETWO, several

modifications to existing codes were required in order to properly treat the ARIES ACT scenarios. These improvements are consequently available for use in future studies. This included modifications to the equilibrium construction in EFIT and processing through the GATO mapping to facilitate the interfacing between the transport codes and the TSC equilibrium modeling; the mapping for the ideal MHD stability code GATO was modified to read the non-standard equilibrium files produced by the TSC code and interpolate to a standard square grid needed for both EFIT and the transport modeling. Also, in the process of reconstructing the Greens Function Tables for ARIES the EFIT code was modernized to F90 since this and this version needed to be ported to the local Linux cluster. The F90 version of the code was made publicly available.

Additionally, the current drive package GENRAY was modified and additional diagnostics were included in the parallelized ONETWO transport code. The ARIES-AT scenario requires multiple frequency LH waves from different launchers. In general, each grill in practice can launch a different frequency wave into the plasma but in the previous version of the GENRAY code, every grill was assumed to launch the same frequency. To model cases such as the 2006 ARIES AT design, separate simulations would be needed for each frequency and the heating and driven current from each grill summed to compute the total. The capability of launching multiple waves with different frequency from each launcher for LH or FW has now been added to the code by including multiple grills in the poloidal plane. In addition to the ICCD and LHCD in ARIES simulations, test runs were done for ECCD scenarios in ITER and LHCD in FDF. The multiple ray tracing option in GENRAY was also released in the public version under the IMFIT interface.

Several improvements were made to enhance the tools being used in the transport simulations. In particular, new diagnostics were implemented to diagnose better the individual species fluxes at any time during the evolution, as in Fig. 14 and Fig. 27. Also, the newest NFREYA neutral beam module was included in the ONETWO simulation code for future use.

3.8. Lessons Learned

A number of features of the simulations performed for the various ARIES design iterations were unanticipated from previous simulation efforts. One major reason for this is the self-heating inherent in the burning plasma scenarios considered. This feature makes the simulations particularly sensitive and a bifurcation is often present where a small change in parameters can result in a sudden change from a self-sustained steady state with excess fusion power output to a complete or partial collapse where the fusion heating is insufficient to sustain the temperature profile above the values needed for fusion reactions to occur. Therefore, in a burning plasma scenario where the plasma is

largely self heated steady state is significantly more difficult to achieve. The profiles tend to collapse completely when insufficient fusion power is supplied. The level required is sensitive to the transport and therefore depends on the model used. In each case, the density appears to be crucial in preventing this collapse. Density needs to be sufficiently high at least in the core where the temperatures are high in order to obtain sufficient fusion power to sustain the temperature. In some cases, notably with the GLF23 model, a density that is too high also appears to result in a runaway state. The mechanism in this case is not entirely clear but appears to be due to steepened gradients as an internal transport barrier forms.

Additionally, the GLF23 transport model is not sufficient for these burning plasmas. Usually, the assumptions inherent in this model result in somewhat optimistic predictions for DIII-D simulations. However, in these cases, GLF23 appears to overestimate the transport. The reason for this is not entirely clear. In the simulations here, this often resulted in a collapse that was not reproduced by the more sophisticated TGLF and Multi-Mode models. Nevertheless, it should be emphasized that even with these models, it is still relatively easy to find cases — for example at low density — that still collapse. It should be noted as well that, while the collapse for higher density may be an artifact of the GLF23 model in the ACT 1A simulations, it seems likely that the same mechanism can operate in the more sophisticated TGLF and Multi-Mode models when the density is too high. In general, analysis of the individual micro-instability contributions is a key tool in diagnosing the reasons for collapse.

The current drive required to sustain q appears to generally be easily achieved in the cases simulated with the specified mix of FW and LH. This appears to be a feature of the ARIES designs, which likely results from the extensive efforts to obtain initial configurations with large and well-aligned bootstrap fractions. However, it must be cautioned that the final steady state temperature profiles are modified and the subsequent iterations to find a self-consistent steady state seems likely to destroy some of the bootstrap current alignment of the initial state. In that case, the current drive requirements will increase. It is not yet clear how much increase will be needed.

3.9 Further Work

Considerable further work is needed to complete this study. The major effort needs to be completion of the fully self-consistent simulations of the final ACT 1 scenario by iterating from the state described in Sec. 3.6 by a second and possibly more transport simulations. Further, the density profile evolution should be included along with a re-evaluation of the current drive requirements to maintain the desired design safety factor profile. This profile may need to be adjusted if those requirements become excessive.

Following this, as described in Fig. 3, optimization with further adjustment of the profiles should be done to improve the fusion power.

Finally, once the code linkages are well defined, the iteration process can be incorporated into the OMFIT framework. Within that system, choices can be made as to which transport model to invoke, and different codes can be selected to test various other features of the configuration such as stability limits to various modes, including low and high n ideal modes, resistive tearing modes, and resistive wall modes requiring possible active stabilization.

4. Meetings

4.1. US Japan Workshops

A presentation was made at the US Japan Workshop on Power Plant Studies held at UCSD on February 24, 2010. The talk covered the vision of an Advanced Tokamak reactor as outlined in the 2009 US DOE ReNeW report [1]. This presentation considered the tokamak as a highly optimized system operating beyond the passive stability limits and actively controlled by a sophisticated control system. The vision is akin to that of a modern fighter aircraft where the performance gains over a passively stable system are similarly very large.

A presentation was also made at the US-Japan Workshop on Fusion Power Plants and Related Advanced Technologies held at UCSD on March 8–9, 2012 on "Progress in Modeling of ARIES ACT Plasma" covering the ARIES work.

4.2. Town Meeting

In conjunction with Mark Tillack (UCSD) and C. Kessel (PPPL), Alan Turnbull co-organized the ARIES Town Meeting on "Edge Plasma Physics and Plasma Material Interactions in the Fusion Power Plant Regime" on May 20 and 21, 2010, at UCSD. The Town Meeting was a follow-on to the High Heat-Flux Workshop previously held at UCSD in December 2008 and had strong participation from Europe and Japan. The focus was on the needs for physics modeling of the edge plasma in a reactor relevant regime. The hope was to foster a serious technical exchange between physicists, modelers, and engineering and materials experts to determine where work is needed that has not been addressed by ITER. This appears to have been accomplished.

Summaries from each of the talks in the Town Meeting were solicited. The sections summarizing the contributions from future devices to the edge plasma and materials interface issues, on the small ELM and ELM-free options, and on edge plasma and plasma-material interface (PMI) concerns for fusion power plants were contributed. For the latter, a comparison table of ITER and DEMO listing key differences that have an impact on the materials interface, such as the total and pedestal stored energy, fluxes of particles, energy, and radiation to the first wall and divertor, etc. was also added. This table may provide a particularly useful resource in future. The complete report was also edited for publication and subsequently published after several iterations in Nuclear Fusion. GA contributed 33% of the publication costs.

4.3. ARIES Presentations

H. St John presented the ACT 1B self-consistent simulation results at the APS meeting in Salt Lake City in November 2011. A summary on ELM-free and small ELM options for a reactor scenario was contributed to a paper summarizing the physics aspects of the ACT-1 design and to be published in Fusion Engineering and Design.

4.4. Additional Technical Contributions

On request from members of the ARIES Team, Gary Jackson extended and generalized an earlier memo on tritium burn-up fractions to include estimates of the burn-up fraction under varying confinement assumptions and in a form suitable for publication. This should clarify much of the confusion on this issue since a number of estimates have been derived based simply on the capacity for tritium handling.

Ken Schultz contributed data to Les Waganer on cost algorithms for turbine generator plants.

References

[1] Research Needs for Magnetic Fusion Energy Sciences, Report of the Research Needs Workshop, Bethesda MD, June 8-12, 2009 (2010)
[2] K.H. Burrell, *et al.*, Phys. Plasmas **12**, 056121 (2005)
[3] M. Greenwald, *et al.*, Phys. Plasmas **6**, 1943 (1999)
[4] T.E. Evans, R.A. Moyer, K.H. Burrell, M.E. Fenstermacher, I. Joseph, A.W. Leonard, T.H. Osborne, G.D. Porter, M.J. Schaffer, P.B. Snyder, P.R. Thomas, J.G. Watkins, and W.P. West, Nat. Phys. **2**, 419 (2006)
[5] A.M. Garofalo, *et al*., Nucl. Fusion **51**, 083018 (2011)
[6] R. Maingi, *et al.*, Phys. Rev. Lett. **103**, 075001 (2009)
[7] R.M. McDermott, *et al.*, Phys. Plasmas **16**, 056103 (2009)
[8] L.R. Baylor, *et al.*, Phys. Rev. Lett. **110**, 245001 (2013)
[9] Y. Kamada, *et al.*, Plasma Phys. Control. Fusion **42**, A247 (2000)
[10] E.J. Doyle, R.J. Groebner, K.H. Burrell, P. Gohil, T. Lehecka, N.C. Luhmann, Jr., H. Matsumoto, T.H. Osborne, W.A. Peebles, and R. Philipona, Phys. Fluids **B3**, 2300 (1991)
[11] L.L. Lao, *et al.*, Nucl. Fusion **41**, 295 (2001)
[12] P.B. Snyder and H.R. Wilson, Plasma Phys. Control. Fusion **45**, 1671 (2003)
[13] L.C. Bernard, F.W. Helton, and R. Moore, Comput. Phys. Commun. **21**, 37 (1981)
[14] L. Degtyarev, A. Martynov, S. Medvedev, F. Troyon, L. Villard, and R. Gruber, Comput. Phys. Commun. **103**, 10 (1997)
[15] R.C. Grimm, J.M. Greene, and J.L. Johnson, in Methods in Computational Physics, Vol. **16**, p. 253, (J. Killeen, Ed., Academic Press, New York) (1976)
[16] P.B. Snyder *et al.*, Phys. Plasmas **9**, 2037 (2002)
[17] W. Suttrop, O. Gruber, S. Gunter, D. Hahn, A. Herrmann, M. Rott, T. Vierle, U. Seidel, M. Sempf, B. Streibl, E. Strumberger, D. Yadikin, O. Neubauer, B. Unterberg, E. Gaio, V. Toigo, P. Brunsell, and ASDEX Upgrade Team, Fusion Eng. Design **84**, 290 (2009)
[18] A.E. Hubbard, *et al.*, "Progress in performance and understanding of steady-state ELM-free I-modes on Alcator C-Mod," 24th IAEA Fusion Energy Conference (2012) paper EX/1-3] (2012)
[19] S.C. Jardin, *et al.*, Fusion Eng. Design **80**, 25 (2006)
[20] G.M. Staebler, J.E. Kinsey and R.E. Waltz, Phys. Plasmas **12**, 102508 (2005)
[21] R.E. Waltz, G.M. Staebler, W. Dorland, *et al.*, Phys. Plasmas **4**, 2482 (1997)
[22] P.B. Snyder, *et al.*, Nucl. Fusion **51**, 103016 (2011)

[23] L. Luo, T Rafiq, and A.H. Kritz, "Improved Multi-mode Anomalous Transport Module for Tokamak Plasmas", to appear in Comput. Phys. Commun., 2013
[24] J.R. Walk, *et al.*, Nucl. Fusion **52**, 063011 (2012)
[25] A.P. Smirnov and R.W. Harvey (rwharvey@compxco.com), Report CompX-2000-01, Ver. 2, http://www.compxco.com/genray.html
[26] L.L. Lao, *et al.,* Nucl. Fusion **30**, 1035 (1990)
[27] W. Pfeiffer, *et al.*, GA-A16278 (1980); https://fusion.gat.com/THEORY/onetwo/
[28] O. Meneghini and L.L. Lao, Plasma Fusion Research **8**, 2403009 (2013)